(Online) ISSN 2744-1741
Defense and Security Studies *Original Research*
Vol. 7, No. 1, 2026, pp.60-88
https://doi.org/10.37868/dss.v7.id309

Analysis of Optical Telescope Element (OTE) used in James Webb Space Telescope (JWST)

Alan Catovic*[1], Dzan Jasarevic
[1] Mechanical Engineering Faculty, University of Sarajevo, Bosnia and Herzegovina

*Corresponding author E-mail: catovic@mef.unsa.ba

Received: Jan. 14, 2026
Revised: Feb. 10, 2026
Accepted: Feb. 12, 2026
Online: Feb. 13, 2026

Abstract

This paper presents an analysis of the James Webb Space Telescope (JWST) Optical Telescope Element (OTE) based on its published optical prescription and system architecture. Using modeling, key optical performance parameters were evaluated, including spot diagrams, footprint diagrams, wavefront error (WFE), point spread function (PSF), Strehl ratio, encircled energy (EE), and modulation transfer function (MTF). The segmented 6.6 m primary mirror was modeled using a User-Defined Aperture (UDA) approach to accurately reproduce the hexagonal pupil geometry and diffraction effects. Results confirm diffraction-limited performance across the evaluated field, with RMS wavefront error well below the Maréchal criterion, high Strehl ratios (≥0.87 off-axis and ≥0.97 on-axis at 1 μm), and encircled energy closely matching the diffraction limit. MTF curves demonstrate strong contrast transfer up to the cutoff spatial frequency with minimal field-dependent degradation.

Additional analyses were performed to assess the impact of individual segment piston and tilt misalignments. Controlled perturbations show that segment-level phase discontinuities significantly degrade WFE, emphasizing the importance of precise segment phasing and wavefront sensing and control (WFS&C).

Keywords: JWST, optical design, segmented mirror, wavefront error, PSF, MTF, encircled energy

1. Introduction and review of the JWST design parameters

The development of the James Webb Space Telescope (JWST) mirror system represents one of the most ambitious optical engineering efforts ever undertaken. JWST emerged from a decades-long evolution of ideas that sought to define a true successor to the Hubble Space Telescope (HST). The origin of the project can be traced to 1985, when Riccardo Giacconi and Pierre Bely at the Space Telescope Science Institute began developing concepts for a "super-HST." Early designs considered 8-10 m monolithic mirrors in geosynchronous orbit, Golay interferometric arrays, and far-infrared telescopes such as the Large Deployable Reflector. These investigations demonstrated that while interferometric arrays offered high resolution, only a compact, cold, single-aperture telescope could achieve the sensitivity required for observing faint galaxies in the infrared. Subsequent studies explored 16 m lunar observatories and 6 m high-Earth-orbit telescopes, but thermal and operational constraints made those approaches impractical.

The turning point came in the mid-1990s, when NASA's Goddard Space Flight Center and STScI engineers, led by John Mather, Pierre Bely, Peter Stockman, and others, defined a concept for a large, deployable infrared

observatory at the Sun-Earth L2 point, where the Sun, Earth, and Moon would remain in a single direction behind a multi-layer sunshield. This configuration offered stable thermal conditions, continuous deep-space viewing, and the ability to passively cool the telescope to below 50 K. The resulting "Yardstick" design (1996) introduced many of JWST's defining features: a segmented beryllium primary mirror (6-8 m class), a three-mirror anastigmat (corrected for spherical abertion, coma and astigmatism) optical layout with a fast-steering mirror for image stabilization, and a diamond-shaped sunshield providing 40-50% instantaneous sky coverage.

This architectural shift required major advances in lightweight cryogenic optics, precision deployment mechanisms, and integrated modeling that coupled optical, thermal, and structural analyses. The team developed detailed feasibility studies and monographs to document key subsystems - sunshield design, stray-light control, mirror actuator placement, and wavefront error budgets - which later guided industrial partners such as Ball Aerospace, TRW, and Lockheed Martin. Iterative refinements reduced the primary mirror to 6.6 m while maintaining full mid-infrared capability. The final design balanced scientific ambition with cost and launch constraints, adhering to NASA's goal of achieving greater capability than HST at comparable total cost [1,7]. Fig. 1 shows a summary of the JWST Observatory.

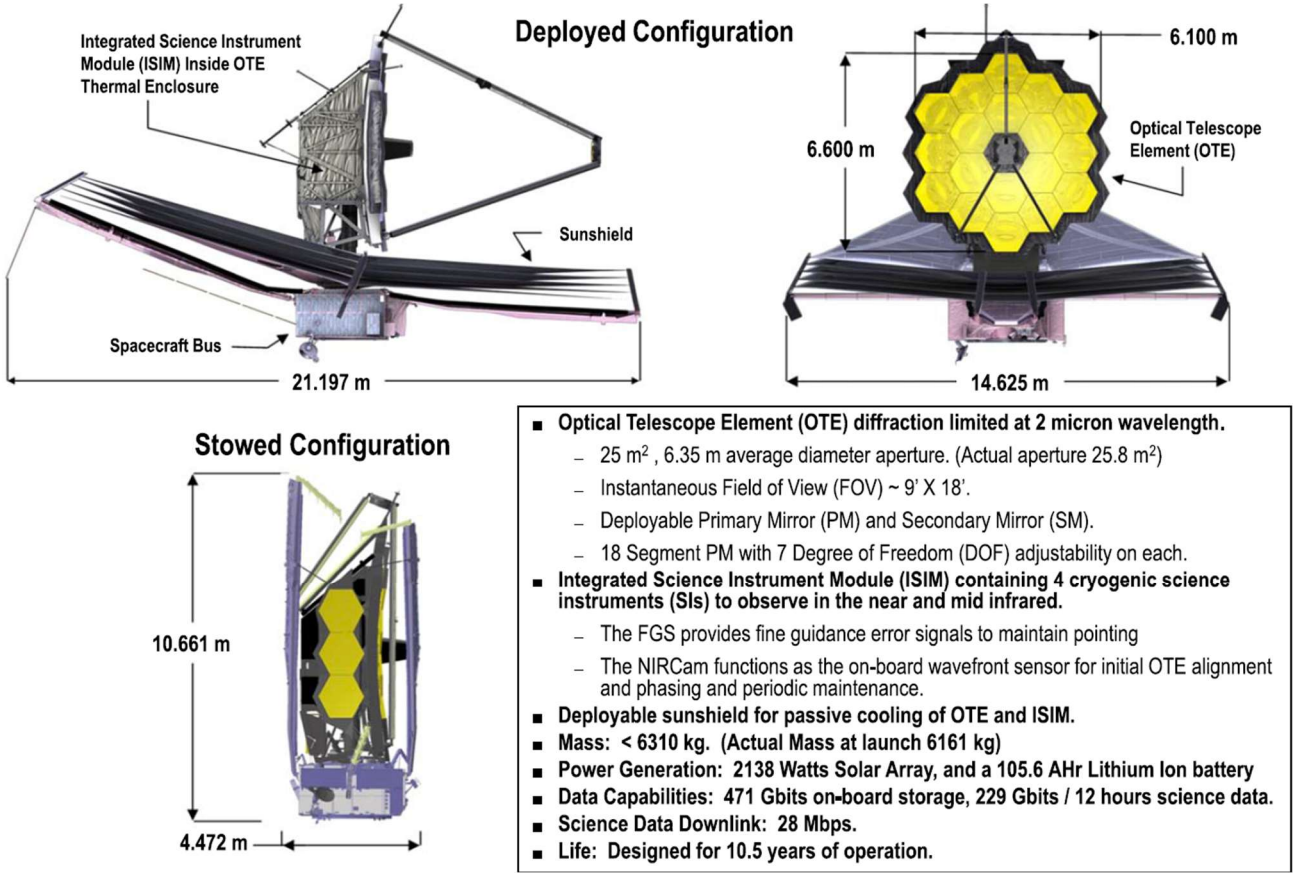

Fig. 1 Summary of the JWST Observatory [3]

The telescope's fundamental mission is to observe the epoch of "first light" - the formation of the earliest stars and galaxies - bridging the observational gap between COBE's study of the cosmic microwave background and HST's exploration of the mature universe. This scientific goal required a large collecting aperture (at least 5-8 m), a wide field of view exceeding 4 arcminutes, diffraction-limited imaging at 2 μm, and operation at cryogenic temperatures [4].

The JWST system architecture is shown in Fig. 2. The figure presents the overall system architecture of the James Webb Space Telescope (JWST), illustrating the sequence from launch aboard the Ariane 5 vehicle through transfer to the Sun–Earth L2 point. It shows key mission phases including upper-stage separation, observatory deployments (solar array, antennas, sunshield, and Optical Telescope Element), and the transfer trajectory to the L2 Lissajous orbit. The diagram also depicts the communications architecture, highlighting S-band and Ka-band telemetry, command, and ranging links between JWST, the Deep Space Network, and mission operations centers, which provide continuous coverage during critical mission events and routine science operations.

Within less than a decade, NASA and its industry partners designed, fabricated, and tested twenty-one beryllium mirrors for the Optical Telescope Element (OTE). This large-scale effort required parallel progress in materials science, cryogenic technology, metrology, and systems integration to produce a lightweight, thermally stable, diffraction-limited telescope capable of operating at 40 K. Early in the program, NASA determined that existing cryogenic mirror technology, such as that used on the Spitzer Space Telescope, could not satisfy JWST's sensitivity and stability requirements. Several demonstration programs were launched, notably the Subscale Beryllium Mirror Demonstrator (SBMD) and the Advanced Mirror System Demonstrator (AMSD). The AMSD Phase 2 and 3 efforts demonstrated that beryllium mirrors could survive vibration and acoustic environments, control fabrication stresses, and maintain figure accuracy through cryogenic cycling - achieving Technology Readiness Level 6, a prerequisite for flight qualification. A formal Mirror Recommendation Board compared beryllium with alternative ultra-low-expansion (ULE) glass designs. Cryogenic test data revealed the decisive advantages of beryllium: high thermal conductivity, low density, and a near-zero coefficient of thermal expansion at cryogenic temperatures. Consequently, beryllium was selected as the baseline material for all OTE mirrors, providing superior stability and reduced mass.

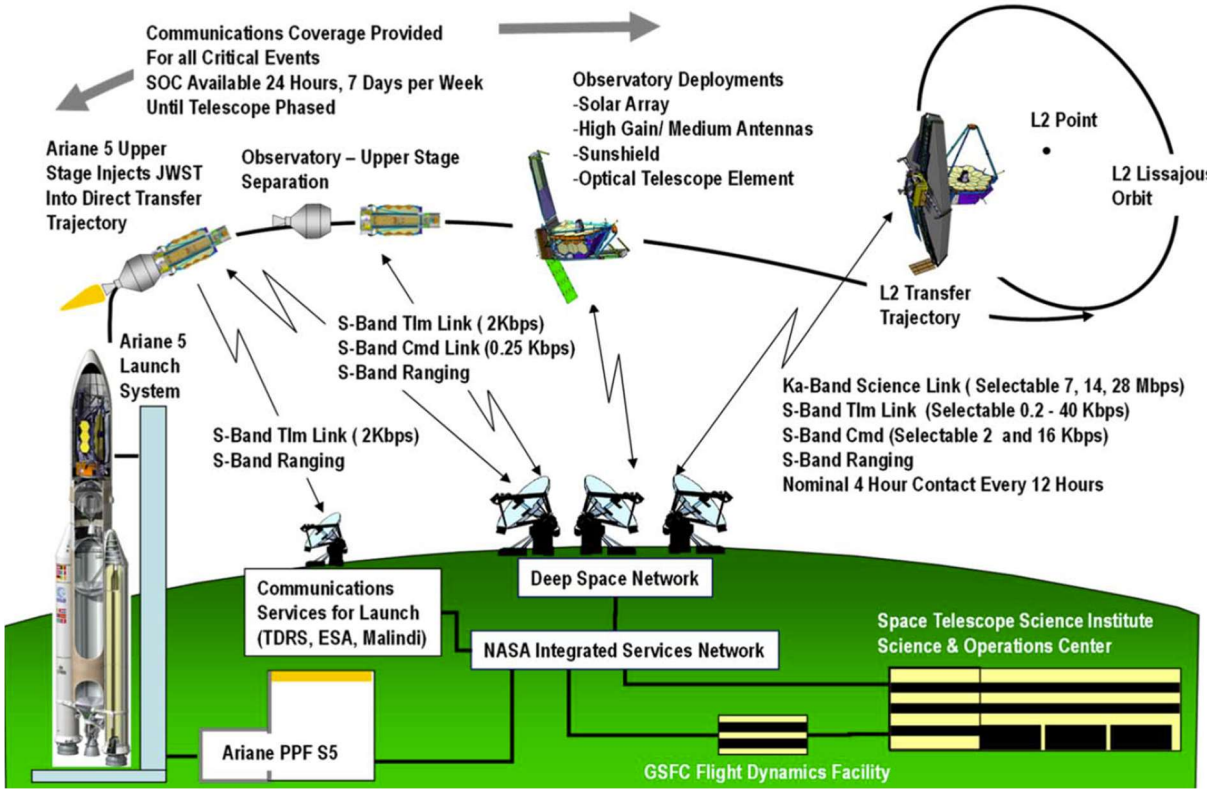

Fig. 2 The JWST system architecture [3]

The program also implemented an extensive risk-management framework early in development. Risks were systematically identified and mitigated, evolving from material-stress and vibration concerns to polishing precision, edge handling, and cryogenic performance. Dedicated engineering development units were built both for the primary and secondary mirrors, serving first as testbeds and later as qualified spares. Mirror fabrication followed a complex, multi-institutional workflow led by Ball Aerospace, with key contributions from Brush Wellman (beryllium blanks), Axsys Technologies (machining), L3-SSG-Tinsley (precision polishing), and NASA's cryogenic test facilities.

The production cycle - from powder-metallurgy beryllium blank to flight-qualified, gold-coated mirror - lasted about 8.5 years. Each segment underwent sequential machining, fine polishing to < 20 nm RMS surface error, cryogenic mapping, coating, vibration testing, and final cryogenic acceptance testing. All 21 flight mirrors met or exceeded their optical specifications. The eighteen primary mirror segments achieved surface figure errors near 25 nm RMS, the secondary and tertiary mirrors about 20 nm, and the fine-steering mirror 15 nm RMS - well within the allocated budgets for achieving a system-level wave-front error of 150 nm RMS. The successful completion of this mirror campaign demonstrated not only the feasibility of large, lightweight, cryogenic optics but also the effectiveness of distributed collaboration among NASA, Northrop Grumman, Ball Aerospace, and numerous subcontractors and laboratories across the United States [2].

The JWST scientific objectives required a cryogenic infrared observatory featuring a 6.6 m deployable primary mirror, operating at temperatures below 55 K and optimized for imaging and spectroscopy from 0.6 μm to 28 μm. Four primary instruments - NIRCam, NIRSpec, MIRI, and FGS/NIRISS - cover this spectral range and provide complementary capabilities for imaging, spectroscopy, and fine guidance. The development of JWST faced five dominant technical challenges. The first was the cryogenic environment, demanding passive cooling through a five-layer sunshield that reduces solar heating by a factor of roughly one million, combined with radiators and an active cryocooler for MIRI operating at 6 K. The second was the deployment challenge: the telescope and its 21×15 m sunshield were too large for any launch vehicle fairing and thus had to be folded for launch and autonomously deployed in space through a complex sequence of over 300 single-point mechanisms. The third challenge was mass limitation, forcing a highly integrated structural architecture where optical, thermal, and electrical interfaces were tightly coupled. The fourth concerned optical stability, which had to be achieved passively - without active adaptive optics - through careful design of beryllium mirror segments, composite support structures, and precise thermal control. Finally, the verification challenge arose because the full observatory could not be tested end-to-end on the ground; instead, its performance had to be verified analytically through an advanced program of Integrated Modeling (IM) linking structural, thermal, optical, and dynamic simulations [3].

Fig. 3 shows the integrated science instrument module. The figure illustrates the architecture and functional segmentation of the Integrated Science Instrument Module (ISIM) of the James Webb Space Telescope (JWST). It highlights three main regions:

(1) the science instruments (NIRCam, NIRSpec, MIRI, and FGS/NIRISS) mounted on the ISIM structure and enclosed within the observatory environment,

(2) the ISIM Electronics Compartment (IEC), which provides mechanically mounted and thermally controlled housing for instrument electronics in close proximity to the instruments, and

(3) the spacecraft Command and Data Handling (ICDH) subsystem, which manages instrument commanding and data interfaces with the observatory.

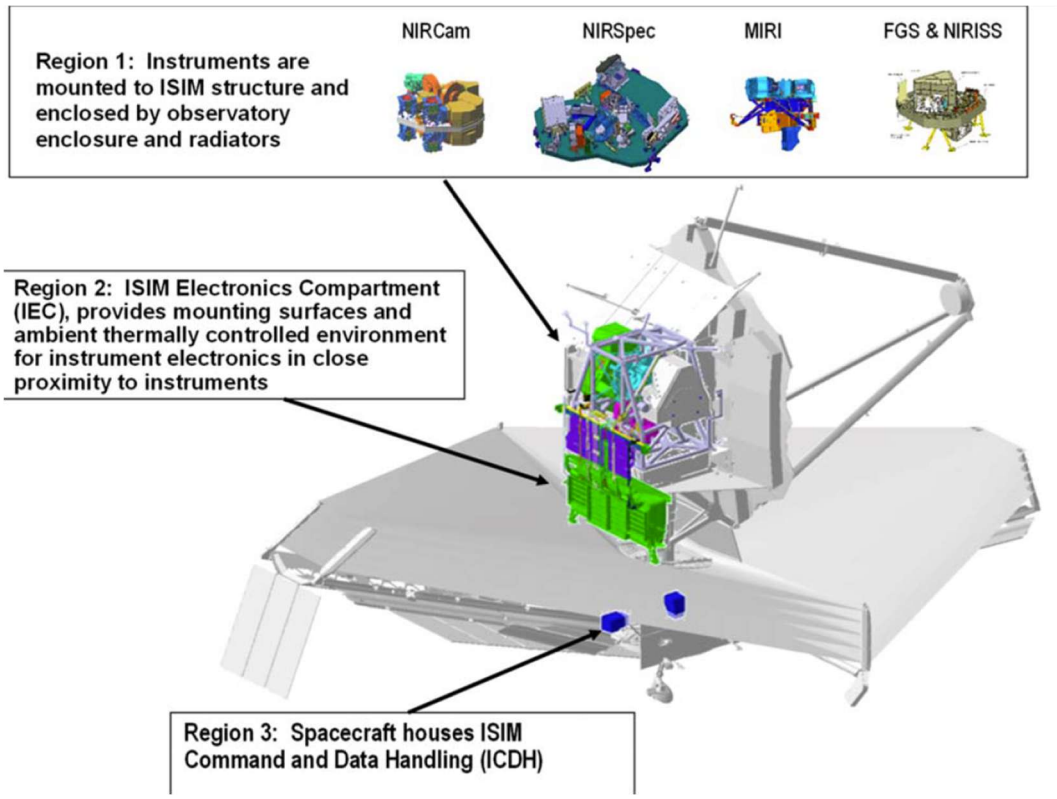

Fig. 3 The integrated science instrument module [3]

The design process relied heavily on analytical verification, marking the first time NASA validated a major observatory primarily through simulation rather than full-scale hardware testing. Integrated modeling coupled finite-element thermal and structural models with optical ray tracing and wave-front control simulations, executed through tools such as NASTRAN and SINDA/TSS (thermal modeling and simulation of complex

spacecraft systems). Each subsystem's model was cross-checked by independent teams from NASA and Northrop Grumman, and validation was performed through subsystem-level tests and correlation against cryogenic chamber experiments. This approach established confidence that the observatory would meet optical and thermal requirements in orbit [3].

Fig. 4 shows the JWST spacecraft bus, highlighting its primary subsystems and thermal-control elements. Visible components include the deployable radiator shade assemblies (horizontal and vertical), the solar array for power generation, station-keeping thrusters, star tracker assemblies for attitude determination, and dedicated equipment panel radiators for heat rejection. Together, these elements support spacecraft power, thermal management, navigation, and long-term stable operation at the Sun–Earth L2 orbit.

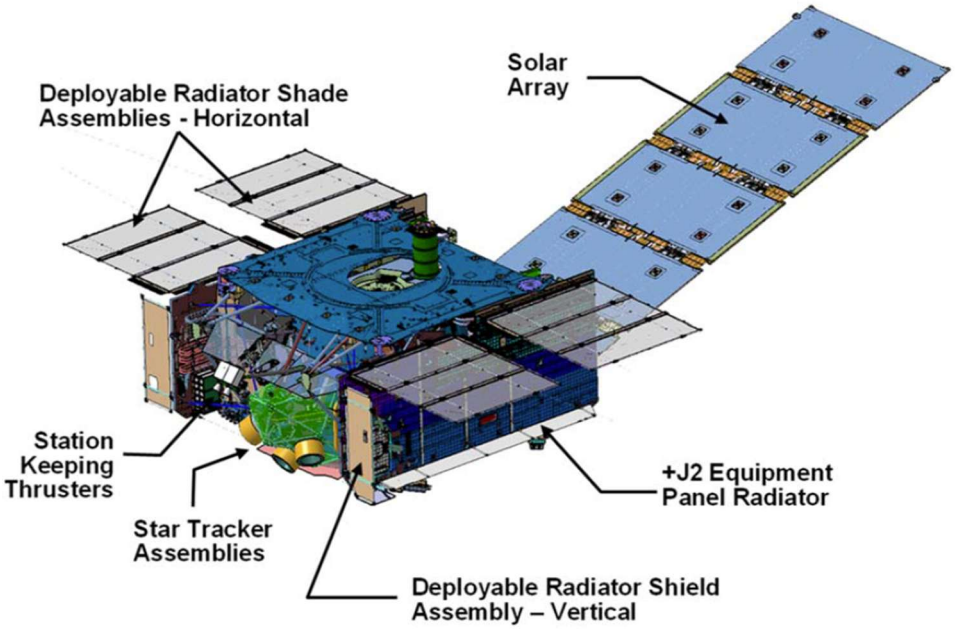

Fig. 4 The JWST spacecraft bus [3]

More information on JWST performance can be found in references [8-20].

Paper [8] provides a status update on the stray-light performance of the JWST Optical Telescope Element. It summarizes the design of baffling, pupil masks, and surface treatments used to suppress off-axis illumination, including analysis of "rogue" and "truant" light paths. The results demonstrate that predicted stray-light levels remain well below detector noise limits across the operational spectral range.

Study [9] presents a comprehensive geometric and radiometric stray-light modeling campaign for JWST. It combines detailed CAD-based ray tracing with sky brightness models to evaluate sensitivity to off-axis sources and scattered light. The analysis validates the effectiveness of the telescope's multi-layer stray-light control strategy and supports on-orbit performance predictions under worst-case illumination scenarios.

Work [10] presents the theoretical foundation and implementation of the wavefront sensing and control (WFS&C) algorithms developed for JWST. It describes phase retrieval, segment phasing, and control-loop strategies used to align the segmented primary mirror and secondary mirror after deployment. The work establishes performance limits, convergence behavior, and robustness of the algorithms under realistic noise and misalignment conditions.

Research [11] analyzes candidate materials for the JWST primary mirror, focusing on thermal stability, stiffness-to-mass ratio, manufacturability, and cryogenic behavior. Beryllium is shown to provide superior performance at cryogenic temperatures due to its low coefficient of thermal expansion and high specific stiffness. The paper documents the rationale behind the final material selection and its impact on optical performance and risk reduction.

Paper [12] defines the optical performance metrics for JWST and evaluates expected image quality in terms of Strehl ratio, encircled energy, and wavefront error. It emphasizes the shift in performance sensitivity from low- to mid-spatial-frequency errors in large segmented telescopes. The study establishes early performance budgets and design trades that guided the OTE architecture.

Work [13] introduces the JWST Optical Simulation Testbed (OST) as a laboratory platform for validating wavefront sensing and control techniques. It presents the testbed architecture, optical design, and initial experimental results. The paper demonstrates the feasibility of ground-based validation for segmented telescope alignment algorithms.

Research [14] details the design of a three-lens anastigmat telescope simulator used within the JWST Optical Simulation Testbed. The simulator accurately reproduces JWST's pupil geometry, aberration structure, and field dependence. The work enables realistic end-to-end testing of wavefront sensing and control algorithms under controlled laboratory conditions.

Study [15] presents the first experimental demonstrations of linear-control alignment for a segmented telescope using the Optical Simulation Testbed. It evaluates convergence speed, robustness, and residual wavefront error under realistic perturbations. The results validate control strategies intended for JWST's on-orbit alignment.

Paper [16] extends previous work to include simultaneous alignment of the primary segmented mirror and secondary mirror. It demonstrates closed-loop control performance and analyzes degeneracies between alignment degrees of freedom. The results directly support JWST strategies and alignment robustness.

Research [17] focuses on wide-field phase retrieval for JWST-like optical systems. It evaluates the accuracy and field dependence of phase-retrieval algorithms across multiple field points. The study supports verification of image quality uniformity and calibration strategies for science instruments.

Paper [18] describes the design and implementation of the Master Optical Reference, a metrology standard used to maintain alignment traceability throughout JWST integration and testing. It ensures consistency between ground measurements and on-orbit optical states. The MOR plays a critical role in reducing alignment uncertainty during assembly and verification.

Paper [19] introduces the Image Quality Verification Analysis (IQVA) framework used to statistically predict JWST's on-orbit optical performance. It combines subsystem test data, structural-thermal-optical modeling, and Monte Carlo simulations. The approach provides confidence bounds on wavefront error and image quality in the absence of full end-to-end testing.

Document [20] defines the operational concept for JWST science missions, including observation planning, calibration, data processing, and wavefront maintenance. It outlines the interaction between spacecraft operations, science instruments, and ground systems. The document provides the operational context in which JWST's optical performance is maintained throughout the mission.

2. Optical parameters of the JWST

Large space telescopes provide enhanced angular resolution and photon-collection capability; however, these advantages require on-orbit deployment as well as active optical alignment and phasing. For segmented-aperture systems such as the James Webb Space Telescope (JWST), image quality is increasingly influenced by mid- and high-spatial-frequency wavefront error (WFE) components, shifting performance emphasis from traditional Strehl ratio metrics toward encircled energy-based criteria [12].

The figure 5 presents an exploded view of the James Webb Space Telescope (JWST) Optical Telescope Element (OTE), illustrating its major structural, optical, thermal, and electronic subsystems. Shown are the primary mirror segment assemblies, the primary mirror backplane assembly, the secondary mirror assembly and support structure, and the Aft Optics Subsystem (AOS). The diagram also highlights the OTE electronics, deployable and fixed ISIM radiators, thermal insulation and light-tight enclosures, stray-light control components, and the deployment tower assembly.

A major innovation of JWST is its capability for remote optical alignment after launch. Because the telescope must be folded for launch and reassembled in orbit, the OTE incorporates a Wavefront Sensing and Control (WFS&C) system within NIRCam. This system executes a four-stage alignment process (Fig. 6): Deployment acquisition - locating each mirror segment and identifying their corresponding image spots; Coarse alignment - adjusting segment curvature and secondary mirror position; Coarse phasing - using the Dispersed Hartmann Sensor to remove piston errors; Fine phasing - achieving nanometer-level wavefront correction through phase retrieval. This process can be repeated periodically throughout the mission to maintain optical performance. Launch-induced motions of the tertiary mirror and science instrument module are the dominant sources of alignment-correctable error, while uncorrectable wavefront errors primarily arise from the surface figure quality

of the mirrors. Optical modeling indicates that figure errors contribute the largest share of total WFE, emphasizing the importance of cryogenic optical manufacturing and test precision. Since both the primary and secondary mirrors are movable but lack direct positional sensors in orbit, degenerate alignment conditions can occur - particularly those combining primary and secondary tilts that yield acceptable on-axis performance but degraded off-axis image quality [4].

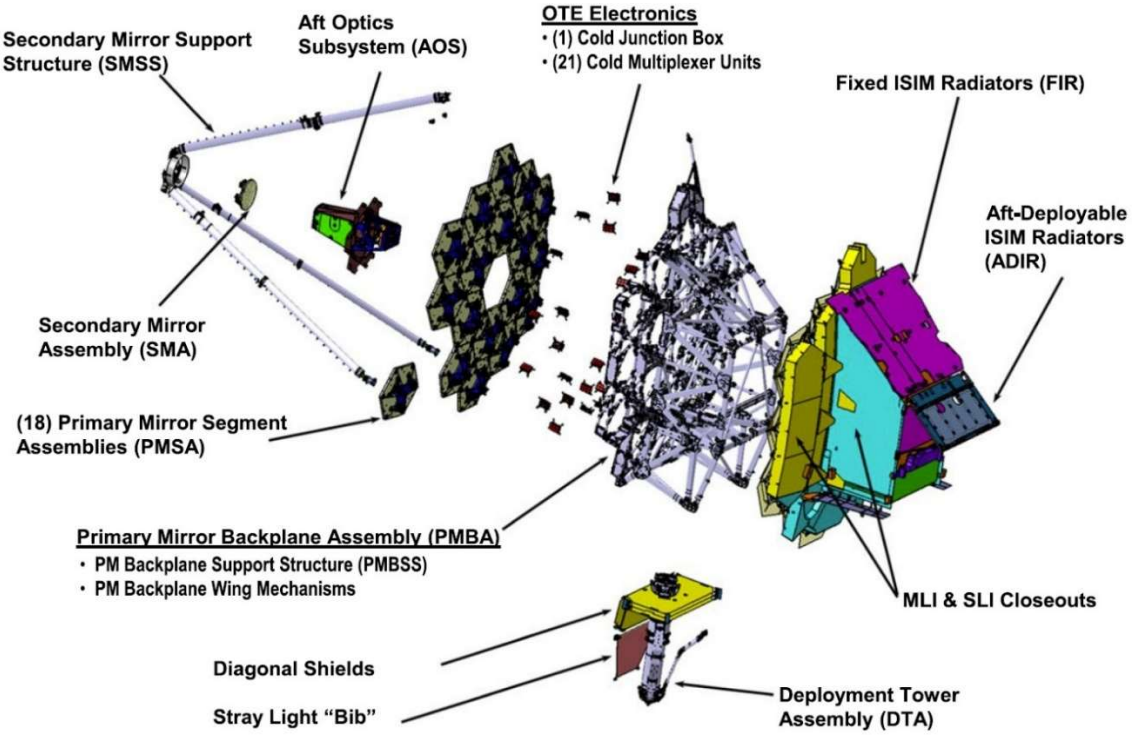

Fig. 5 Optical system of JWST [3]

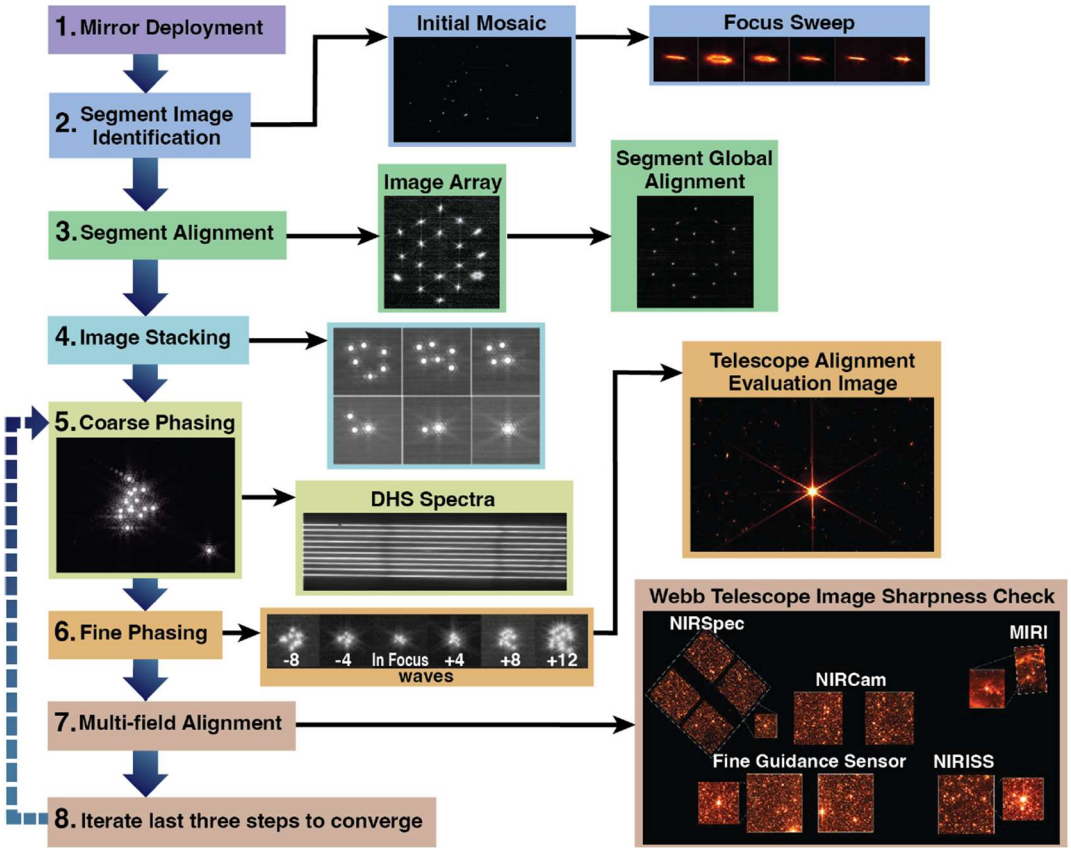

Fig. 6 An overview of the sequence of events during OTE commissioning, including representative examples of flight data [6]

Three primary sensitivity analyses are performed for on-orbit alignment. The first addresses the fundamental alignment process, considering all available compensation degrees of freedom and representing the largest perturbations within the capture range of fine phasing. The second evaluates alignment drift, assessing the impact of slowly varying positional changes that are corrected through periodic realignments, thereby informing alignment update intervals and observational efficiency. The third examines vibration effects, representing uncompensated high-frequency motions of optical elements beyond FSM-stabilized line-of-sight jitter. Each analysis employs a distinct set of sensitivity derivatives tailored to the corresponding perturbation levels and compensators [4].

2.1 Optical Telescope Element (OTE) design

JWST employs a three-mirror anastigmat (TMA) optical configuration operating on-axis in aperture and off-axis in field. Unlike most classical Cassegrain telescopes, the primary mirror (Fig. 7) is an ellipsoidal f/1.2 surface, optimized to reduce spherical aberration and field curvature while enabling a compact, deployable architecture. The 6.6 m segmented primary mirror consists of eighteen hexagonal beryllium segments with gold coatings and protective SiO_2 overlayers, providing reflectivity exceeding 97% for wavelengths above 1 μm.

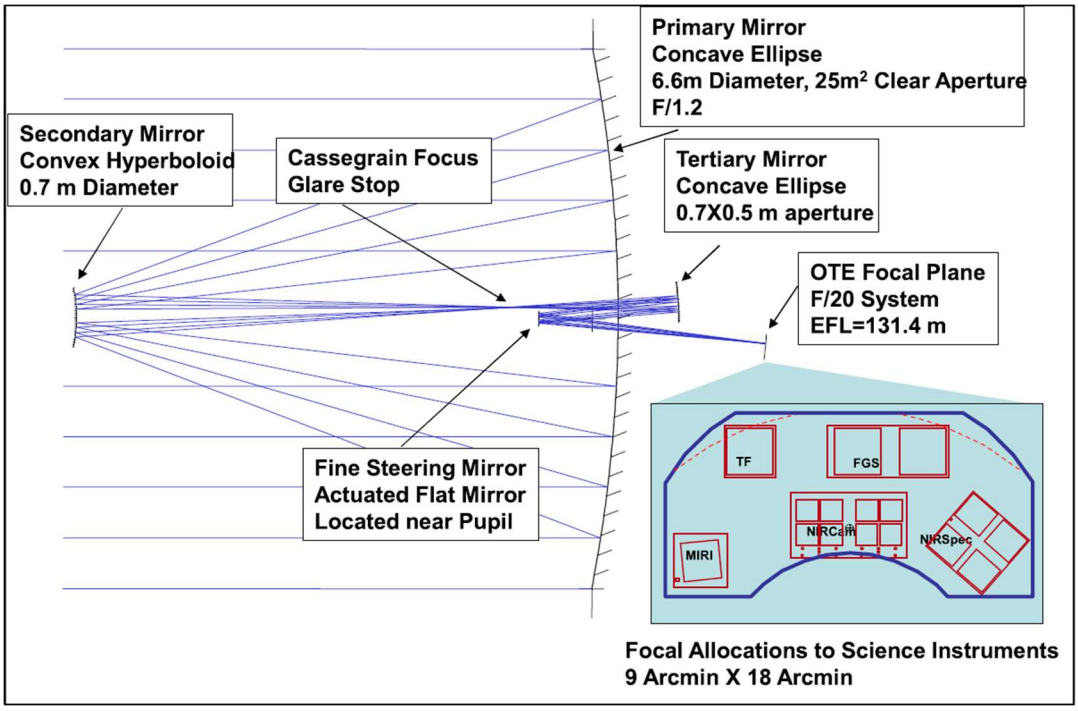

Fig. 7 JWST OTE ray trace and components data [3]

The convex hyperbolic secondary mirror (0.738 m diameter, f/9), mounted on a deployable tripod, forms an intermediate image near the primary mirror vertex of the JWST . The concave elliptical tertiary mirror, housed within the Aft Optics Subsystem (AOS), reimages the pupil to the Fine Steering Mirror (FSM) and generates a common curved focal surface shared by all science instruments. The telescope has an effective focal length of 131.4 m (f/20).

The OTE functions as a reimaging system, intentionally placing the entrance pupil at the primary mirror and forming a real exit pupil within the AOS. This configuration enhances stray-light suppression and pointing stability. The FSM, located near the pupil plane, stabilizes the line of sight and compensates for spacecraft jitter. Partial vignetting of the nominal 18′ × 9′ FOV by the FSM is employed to reduce differential distortion and WFE. Static field distortion is calibrated, while differential distortion due to jitter is minimized through optical design optimization [3].

The JWST mirrors are actively controlled using a hexapod actuation system (Fig. 8), with actuators in each leg providing sub-10 nm positioning resolution and a stroke exceeding 17.5 mm. The figure shows a rear view of a James Webb Space Telescope (JWST) primary mirror segment assembly (PMSA), highlighting the mechanical and actuation architecture used for active optical control. Visible components include the radius-of-curvature (RoC) actuator, beryllium RoC support struts, and the six-degree-of-freedom hexapod actuators that provide precise rigid-body positioning of the mirror segment. The image also identifies the beryllium mirror substrate,

whiffletree support system, delta frame, and backplane interface flexures, which together ensure structural stability while allowing nanometer-scale adjustments. This assembly enables accurate figure control, alignment, and phasing of each primary mirror segment under cryogenic operating conditions.

Three of the six degrees of freedom of each Primary Mirror Segment Assembly (PMSA) have only a weak effect on the wavefront, therefore, up to three actuator failures can occur before a given segment produces a significant impact on the overall wavefront error (WFE). In addition, any small wavefront error introduced by a single segment is averaged with the contributions from the remaining 17 segments, thereby reducing its impact on the overall Strehl ratio and encircled energy (EE) [5].

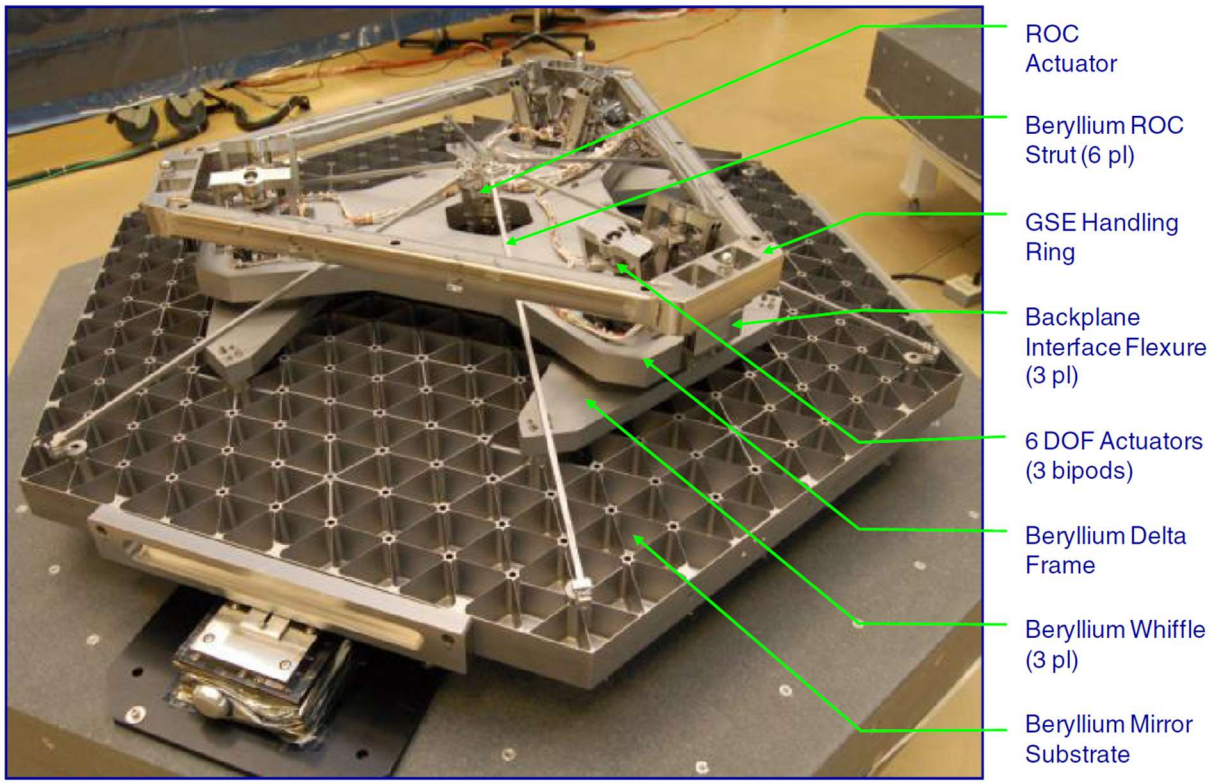

Fig. 8 The rear view of a primary mirror segment assembly, highlighting the radius-of-curvature actuation mechanisms and the rigid-body hexapod positioning system [5]

2.2 Image quality requirements

The primary image-quality requirement (MR-110) specifies a Strehl ratio ≥ 0.8 at 2 μm over the NIRCam field, corresponding to a total system WFE budget of 150 nm RMS. This budget is allocated among static optical errors, thermal distortions, dynamic disturbances, image motion, and system margin.

JWST's image-quality assessment relies on a hierarchy of PSF-derived metrics, including Strehl ratio, encircled energy (EE), anisotropy, and temporal stability. Performance requirements include EE > 0.74 at 1 μm, effective anisotropy < 1% at 2 μm, and EE stability < 2% over time. These complementary metrics avoid oversimplified single-parameter evaluations and are particularly suited to segmented-aperture systems.

Wavefront error is categorized into three spatial-frequency domains:

- Low-frequency (0-5 cycles/aperture): alignment and large-scale aberrations, actively corrected by Wavefront Sensing and Control (WFS&C).
- Mid-frequency (5-30 c/a): segment-level figure and curvature errors, partially correctable.
- High-frequency (>30 c/a): micro-roughness and polishing residuals, uncorrectable in orbit.

This distribution shifts performance sensitivity from Strehl ratio toward encircled energy, emphasizing mid-spatial-frequency control for large segmented telescopes.

Table 1 shows the key optical performance requirements of the JWST and compares them with the measured on-orbit values, demonstrating that the observatory meets or exceeds all major criteria. Specifically, it shows that the effective optical collecting area exceeds the required 25 m², achieving 25.44 m². The image quality,

quantified by the Strehl ratio, surpasses the requirement of 0.8 for both NIRCam at 2.0 μm and MIRI at 5.6 μm. The temporal stability of the point spread function, expressed through encircled energy stability over 24-hour and 14-day intervals, is significantly better than required, indicating excellent wavefront and pointing stability. Also, the telescope exhibits no vignetting across the specified fields of view.

Table 1 Optical Requirements for the JWST [6]

Optical Requirement	Requirement	Measured
Optical Area (m^2)	> 25.0	25.44
Strehl ratio over NIRCam FOV at 2.0 μm	> 0.8	0.84
Strehl ratio over MIRI FOV at 5.6 μm	> 0.8	0.92
Encircled Energy Stability over 24 hours	< 2%	0.2%
Encircled Energy Stability over 14 hours	< 3%	0.53%
Vignetting	None	None

At the observatory level, the JWST optical architecture is designed to satisfy mission science requirements by optimizing image quality-quantified by the Strehl ratio and WFE - across an 18′ × 9′ field of view (FOV), while simultaneously maximizing optical throughput, expressed as the product of collecting area and transmission (A × T), and minimizing stray light.

Figure 9 shows the FOV allocation to the five science instruments, as well as the boundaries of the unvignetted FOV and optimum performance region. The optimum performance region corresponds to the 25 nm nominal design contour. Since the design is restricted to conic mirrors sharing a common tilt axis, the performance is a smooth function of FOV about the parent optical axis. This fact, combined with the nonlinearity of the dominant residual aberration (astigmatism), gives rise to the steep increase in WFE at the upper corners of the FOV [4].

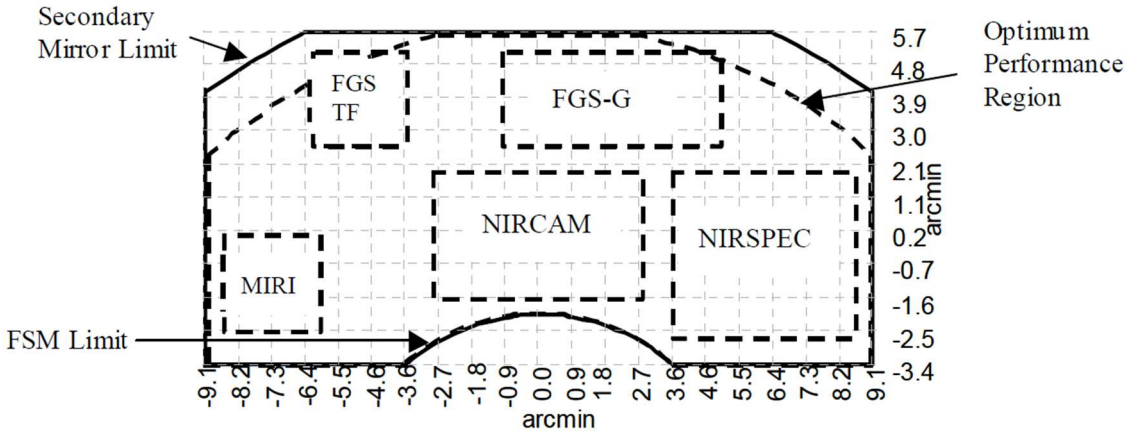

Fig. 9 OTE FOV Allocation [4]

2.3 Thermal stability, and stray-light performance

Thermal stability is achieved through passive cooling and material selection. Beryllium optics and a carbon-fiber composite structure provide low coefficients of thermal expansion and high rigidity at cryogenic temperatures. The five-layer Kapton E sunshield reflects over 200 kW of solar energy, maintaining the telescope near 40 K with significant thermal margin.

The figure 10 depicts the deployable structural architecture of the James Webb Space Telescope (JWST), focusing on the primary mirror support structure and sunshield support system. It illustrates the forward and aft structural assemblies, bipod launch lock mechanisms, spreader bars, membrane assemblies, and articulated boom and linkage systems that enable deployment after launch. The diagram also indicates key structural dimensions and highlights components responsible for maintaining alignment, stability, and momentum balance of the observatory in its fully deployed configuration [4].

Stray-light suppression employs a multi-layered approach, including geometric baffling, a Lyot stop integrated with the FSM, internal instrument masking, and the primary mirror frill baffle. Warm-side optical surfaces are black-coated to reduce mid-infrared emission. Modeling and on-orbit measurements confirm stray-light levels well below detector noise thresholds, even in high-background regions [5][7][8][9].

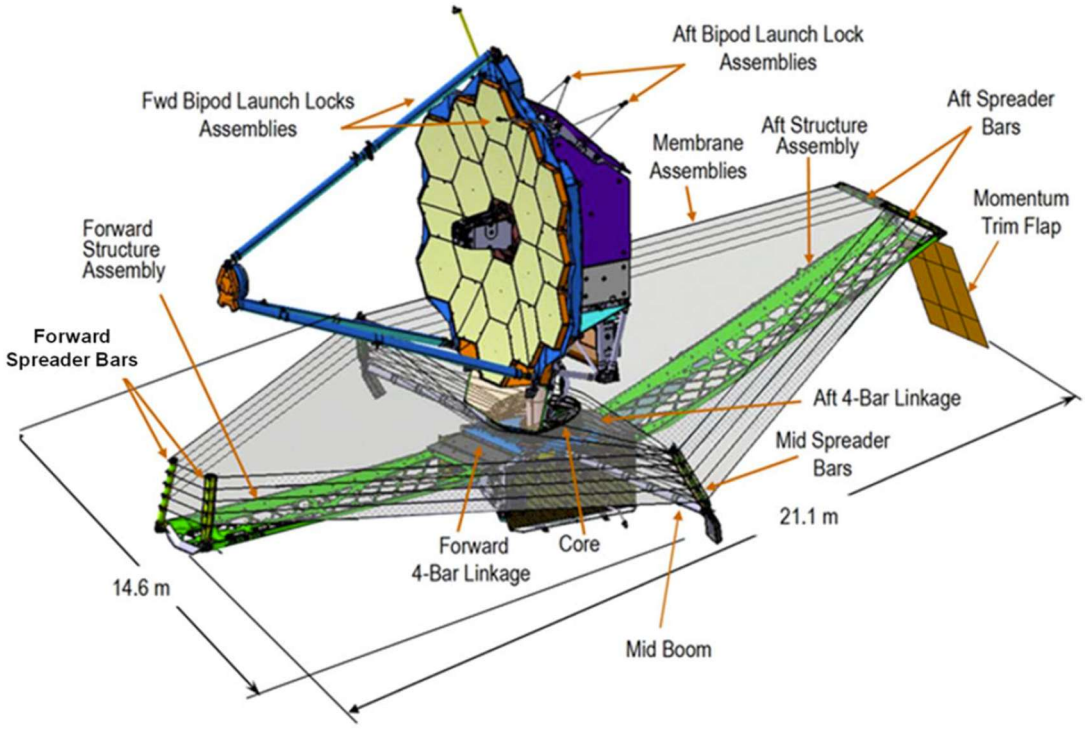

Fig. 10 The JWST sunshield design [3]

2.4 Optical throughput

The telescope's performance metric is the optical throughput per solid angle, defined by the product of collecting area and transmission (A×T). Optical throughput varies from approximately 15.4 m² at 0.8 μm to ~22 m² above 5 μm, accounting for time-dependent contamination effects. The polished areas of the 18 primary mirror segments provide a collecting area exceeding 25 m², and the overall transmission is set by the combined reflectivity of the primary, secondary, tertiary, and fine-steering mirrors. Protected gold coatings establish high reflectivity, remaining nearly constant for wavelengths above 2 μm, with only minor spectral features. The telescope operates over a 0.6-29 μm spectral range. Wavelength-dependent transmission ranges from 0.786 at 0.8 μm to 0.933 at 28 μm, exceeding performance requirements across the full band [3][5].

Molecular contamination is expected from three sources: cleanroom hydrocarbons accumulated during integration, UV-induced amorphous carbon formed in flight, and molecular water that may condense during cooldown. Analyses indicate that hydrocarbon and amorphous carbon levels remain very low, while potential water ice accumulation is mitigated through thermal control, including active heating of the fine steering mirror. Thin contamination layers are shown to have a negligible effect on reflectance across the near-infrared band.

Particulate contamination primarily affects scattering and stray light rather than throughput and is controlled through cleanroom integration and protective handling procedures. The effects of micrometeoroid impacts in the L2 environment were experimentally evaluated and found to cause only microscopic surface pitting, with a cumulative impact area well below 0.1% over a 10-year mission. Combined analyses demonstrate that contamination and micrometeoroid damage result in negligible degradation of JWST's optical throughput over the mission lifetime.

2.5 Wavefront sensing, control, and verification

JWST uses an active Wavefront Sensing and Control (WFS&C) system implemented through NIRCam to align and phase the telescope after deployment. Alignment is performed in four stages—deployment acquisition, coarse alignment, coarse phasing, and fine phasing—achieving nanometer-level precision and repeated periodically during the mission.

Optical verification relied on subsystem testing and integrated modeling, as full end-to-end ground testing was not possible. The Image Quality Verification Analysis (IQVA) framework combined structural-thermal-optical models, WFS&C algorithms, and Monte Carlo simulations (>200 cases) to predict post-launch performance. Results showed that the Optical Telescope Element (OTE) wavefront error meets the 131 nm RMS requirement with 95% confidence, typically within 1–2 nm of predictions.

JWST meets its optical performance requirements, including Strehl ratio ≥ 0.8 at 2 μm and 5.6 μm, encircled energy stability < 2–3%, and effective collecting area > 25 m². Cryogenic polishing, carbon-fiber structural stability, and vibration isolation ensure long-term wavefront stability and diffraction-limited performance throughout science operations.

Geometric susceptibility mapping and sky brightness convolution models confirm that stray light levels remain well below detector noise thresholds, even when observing near bright galactic regions [5]. Fig. 11 shows a high-level overview of the telescope integration and testing sequence from assembly through launch.

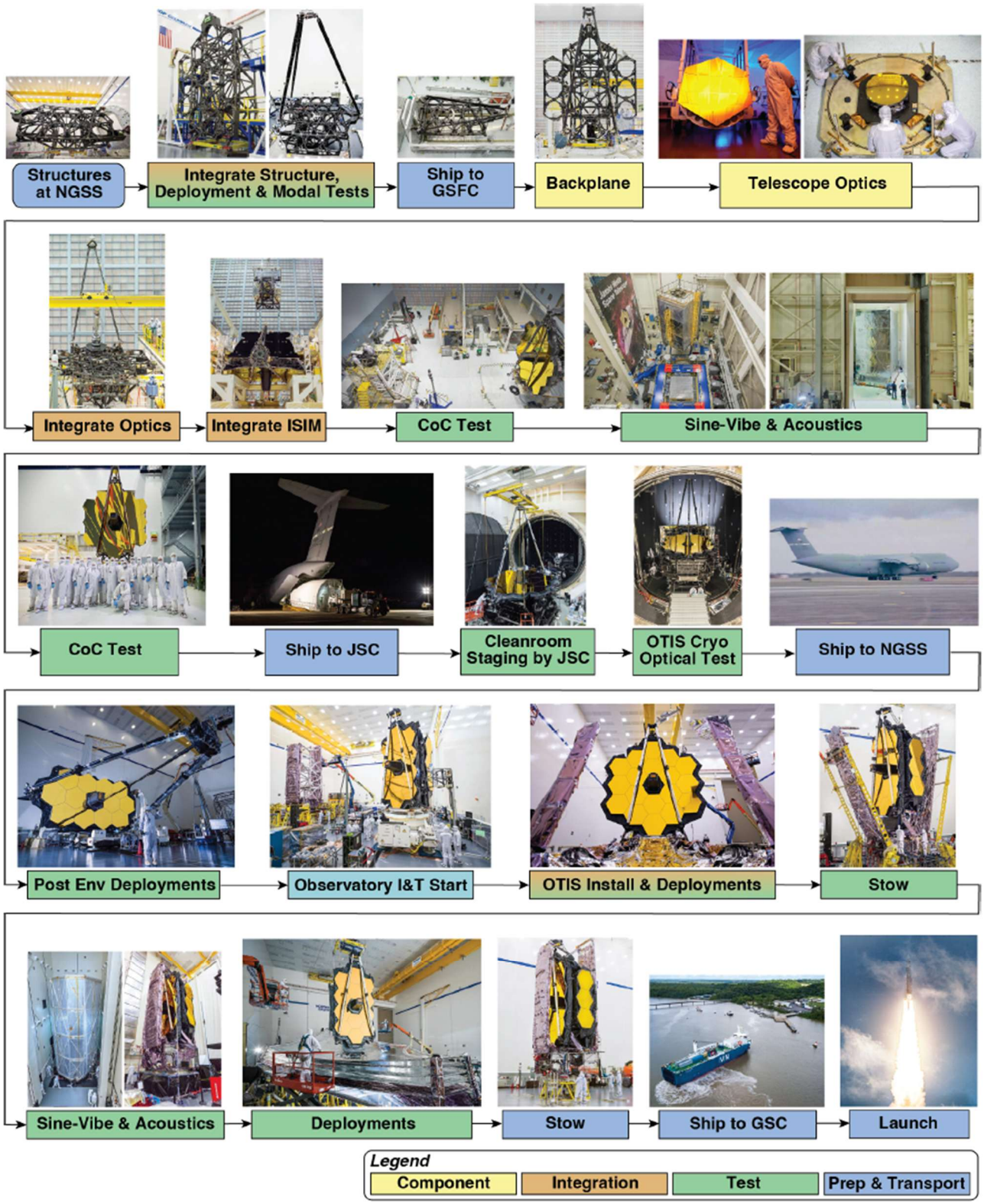

Fig. 11 An overview of the telescope integration and testing sequence from assembly through launch [6]

Fig. 12 presents the surface figure error for the 18 mirrors as measured during acceptance testing, including individual segment RMS values, with an overall RMS of approximately 23 nm and a peak-to-valley value of about 52 nm. The results demonstrate that the mirrors meet the stringent surface accuracy requirements under cryogenic conditions, confirming that the primary mirror achieves the optical quality necessary for JWST's wavefront error budget and diffraction-limited performance after on-orbit alignment and phasing.

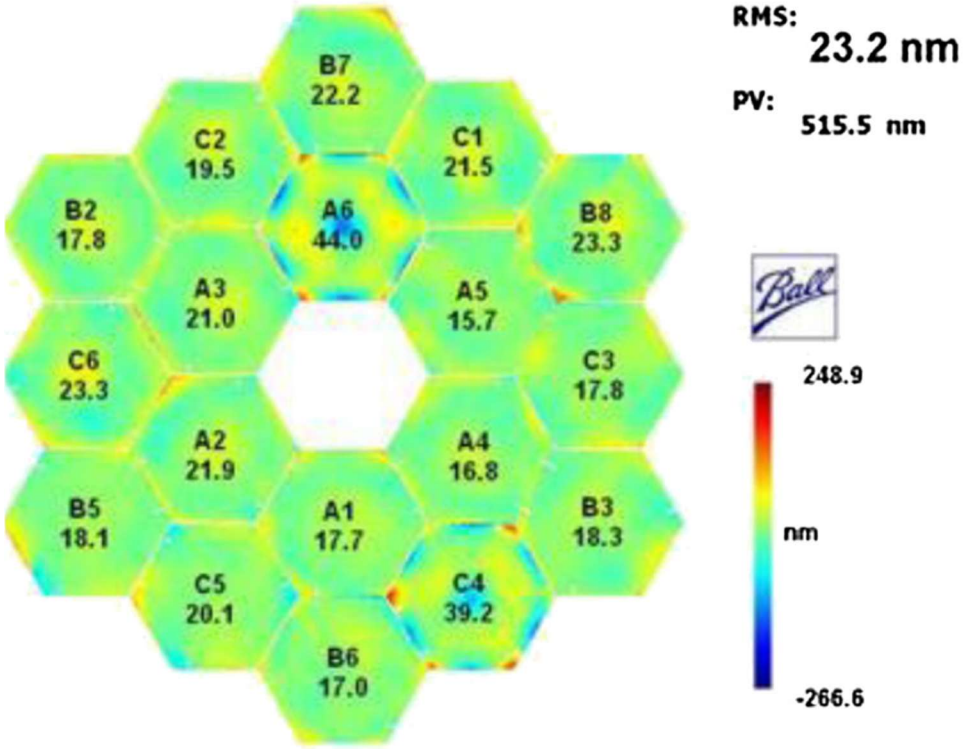

Fig. 12 Primary mirror segment performance after polishing [5]

The figure 13 shows the relative contributions of different tolerance error sources to the overall wavefront error budget of the James Webb Space Telescope (JWST) for each science instrument (NIRCam, MIRI, NIRSpec, FGS-TF, and FGS Guider). The bar chart compares the fractional impact of residual alignment errors, rigid-body motions (RBM), prescription errors, alignment drift, vibration effects, and mirror figure errors. The results indicate that mirror figure error is the dominant contributor to the total wavefront error across all instruments, while contributions from vibration, drift, and rigid-body misalignments are significantly smaller. This distribution demonstrates that JWST's active alignment and stabilization systems effectively control low-frequency and dynamic errors, leaving surface figure quality as the primary limiting factor for optical performance.

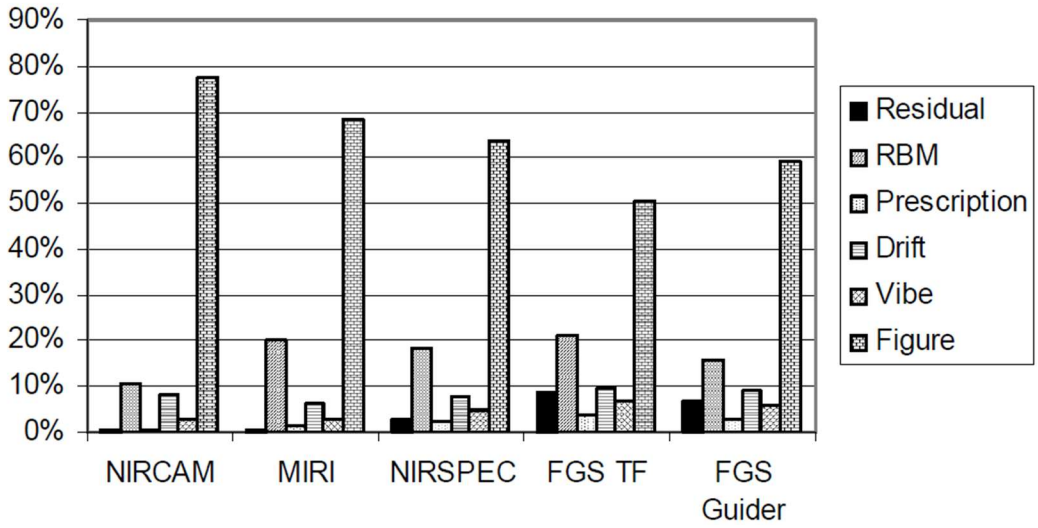

Fig. 13 Primary mirror segment performance after polishing [4]

3. Analysis of optical parameters for JWST

In this paper, several optical parameters of the JWST Optical Telescope Element (OTE) are analyzed: spot diagrams, footprint digrams, wavefront errors (WFE), point spread function (PSF), Strehl ratio, encircled energy (EE) and modulation transfer function (MTF).

Fig. 14 shows screenshot of the optical prescription data for the James Webb Space Telescope (JWST) Optical Telescope Element (OTE), used in this research. Similar data can also be found in [5][6][7][21][22].

	Surface Type	Comment	Radius	Thickness	Material	Coating	Semi-Diameter	Mech Semi-Dia	Conic
0	OBJECT Standard		Infinity	Infinity			Infinity	Infinity	0.000
1	Coordinate Break	field bias		0.000	-		0.000	-	
2	Standard	plot begin	Infinity	1.000E+04			3343.389	3343.389	0.000
3	STOP (aper) Standard	primary	-1.588E+04	-7169.000	MIRROR		3302.600	-	-0.997
4	(aper) Standard	secondary	-1778.900	7965.300	MIRROR		354.464	400.000	-1.660
5	(aper) Standard	tertiary	-3016.200	-1844.100	MIRROR		497.788	-	-0.659
6	(aper) Standard	ne steering mirror	Infinity	0.000	MIRROR		81.217	90.000	0.000
7	Coordinate Break			3027.689 V	-		0.000	-	
8	IMAGE (aper) Standard	image plane	-3039.788 V	-			391.039	-	0.000

Fig. 14 JWST optical prescription

Data in Fig. 14 shows:

- System geometry and layout: The sequence of components, including the apertures (EPD = 6605,2 mm), stops (at primary mirror), mirrors (4 mirrors in total), and image surface, together with their radii of curvature and axial distances. Wavelength chosen was 1 μm, with fields (Fig. 16) representing rectangular FOW of 18′ × 9′ (nominal FOV of the FSM) and effective focal length of 132812 mm.
- Optical elements: The segmented primary mirror, the convex secondary mirror, the concave tertiary mirror, and the fine steering mirror (FSM), each defined as reflective surfaces with their curvatures, conic constants, and clear apertures. From the prescription in Fig. 14 it can be seen that the conic constants (K) are: primary mirror (PM): K = −0.997 prolate ellipsoid (very close to a paraboloid, since $K \approx -1$), secondary mirror (SM): K = −1.660 hyperboloid (because K < −1), tertiary mirror (TM): K = −0.659 prolate ellipsoid (because $-1 < K < 0$). Mirror fabrication considerations were also a driving reason to restrict the mirror contours to conic sections with no higher order aspheric departure [4].
- Apertures are defined as follows: circular for image plane (90 mm radius), rectangular for tertiary mirror (350 × 250 mm), circular for secondary mirror (400 mm radius) and segmented aperture for primary mirror. The prescription includes an aperture definition (user defined aperture file - UDA , Fig. 15) representing the 18 hexagonal primary mirror segments. Each mirror segment is defined as regular hexagon specified by its center coordinates in the pupil plane, its circumscribed radius corresponding to a 1.49 m flat-to-flat segment size, the number of polygon sides (6), and a zero rotational offset. The segments are arranged in five vertical columns with appropriate lateral and vertical offsets to reproduce the full 18-segment JWST primary mirror layout, including the central opening and inter-segment gaps. UDA-based pupil file enables modeling of diffraction effects, wavefront propagation, point spread function formation, and optical performance metrics such as MTF, encircled energy, and Strehl ratio.

```
!Leftmost column of segments, 1-3
POL -2250 1299 745 6 0
POL -2250 0 745 6 0
POL -2250 -1299 745 6 0

!Column left of center, segments 4-7
POL -1125 1949 745 6 0
POL -1125 650 745 6 0
POL -1125 -650 745 6 0
POL -1125 -1949 745 6 0

!Center column, segments 8-12
POL 0 2598 745 6 0
POL 0 1299 745 6 0
POL 0 0 745 6 0
POL 0 -1299 745 6 0
POL 0 -2598 745 6 0

!Column right of center, segments 13-16
POL 1125 1949 745 6 0
POL 1125 650 745 6 0
POL 1125 -650 745 6 0
POL 1125 -1949 745 6 0

!Column rightmost of center, segments 17-19
POL 2250 1299 745 6 0
POL 2250 0 745 6 0
POL 2250 -1299 745 6 0
```

Fig. 15 UDA file for defining18 hexagonal primary mirror segments [22]

X Angle (°)	Y Angle (°)	Weight	VDX	VDY	VCX	VCY	TAN
0.000	0.000	1.000	0.000	0.000	0.000	0.000	0.000
-0.152	0.000	1.000	0.000	0.000	0.000	0.000	0.000
0.152	0.000	1.000	0.000	0.000	0.000	0.000	0.000
0.000	-0.076	1.000	0.000	0.000	0.000	0.000	0.000
0.000	0.076	1.000	0.000	0.000	0.000	0.000	0.000
-0.152	-0.076	1.000	0.000	0.000	0.000	0.000	0.000
-0.152	0.076	1.000	0.000	0.000	0.000	0.000	0.000
0.152	-0.076	1.000	0.000	0.000	0.000	0.000	0.000
0.152	0.076	1.000	0.000	0.000	0.000	0.000	0.000

Fig. 16. Field points defined for JWST OTE model (represent rectangular FOV of 18′ × 9′)

It should be noted that the JWST does not have a single, uniform field of view; instead, its usable FOV is instrument-dependent. The telescope is optimized for high image quality over modest angular fields rather than wide-field surveys. NIRCam, the primary imager and wavefront sensor, provides a combined field of about 2.2′ × 9.7′ across its two modules. NIRSpec offers a field of roughly 3.4′ × 3.6′ for multi-object spectroscopy, MIRI provides an imaging field of about 1.25′ × 1.88′, and the Fine Guidance Sensor (FGS) covers approximately 2.2′ × 2.2′ for precise pointing control. In system-level optical analyses and modeling, a larger notional field (e.g., 18′ × 9′, or 0.30° × 0.15°) can be referenced to assess distortion, pupil behavior, or alignment sensitivity; however, this does not correspond to a single detector's active imaging area.

The figure 17 shows a geometrical ray-trace visualization of the James Webb Space Telescope Optical Telescope Element (OTE), based on data from Fig. 14. Parallel incoming rays from an off-axis field are reflected by the segmented primary mirror (shown as hexagonal elements), redirected to the secondary mirror, and then folded by the tertiary mirror and Fine Steering Mirror toward the final image plane. The different ray colors represent multiple field points and wavelength of 1 μm, illustrating how the three-mirror anastigmat configuration collects and focuses light.

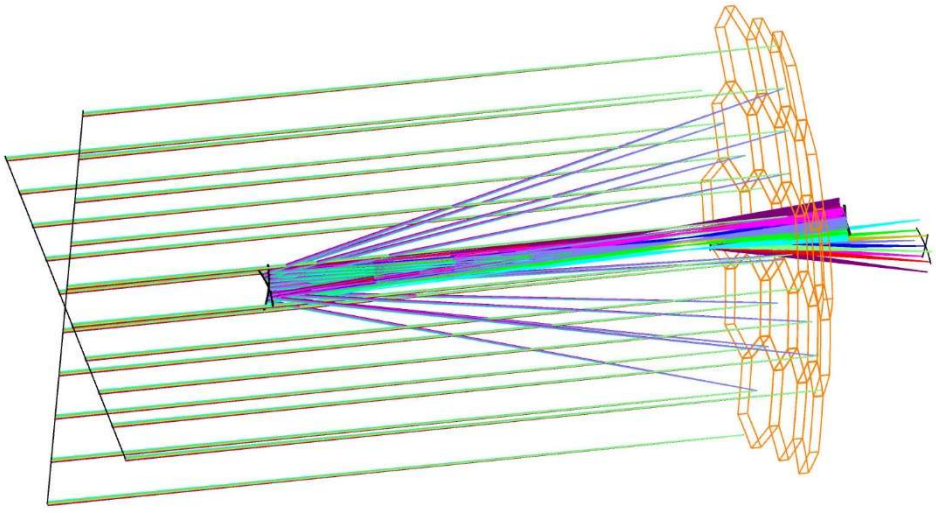

Fig. 17 Geometrical ray-trace visualization of OTE for JWST

Light from the stars is collected by the primary mirror, reflected to the secondary mirror, and then directed to the tertiary and fine steering mirrors before reaching the image plane. Although the ray paths appear to pass through intermediate mirrors in the schematic, this behavior is accounted for by applying a field bias (Fig. 14), which places the nominal on-axis field slightly off-axis. In the Lens Data Editor, this is implemented using a Coordinate Break surface with a small tilt about the X-axis (0.16°), introducing a constant angular offset for the entire telescope and enabling the correct folded optical geometry.

To accommodate off-axis field points and improve focus, the image plane is modeled as a curved surface (Fig. 17) by setting both its radius and thickness as variable parameters. This allows the image surface to adopt a radius of curvature that matches the telescope's inherent field curvature, thereby reducing defocus across the field.

3.1 Analysis of footprint diagrams

Generally, the footprint diagrams are important because they verify there is no loss of light due to vignetting and ensure that components are properly sized to intercept the full optical beam. They play a key role in stray-light analysis by showing where rays interact with optical surfaces, identifying potential sources of unwanted scattering.

Fig. 18 shows the footprint diagram of the JWST optical system at the image location for different field points (shown earlier in Fig. 16). This footprint diagram at the image plane shows how rays from several different field points are distributed across the detector area of the JWST optical system. Each marker corresponds to a specific field position, and their separation indicates the mapping of field angles to distinct image locations, confirming proper field separation and imaging geometry. The footprints remain well contained within the defined image boundary, which indicates correct sizing and placement of the image surface, absence of vignetting at the image plane, and consistent optical alignment across the evaluated field points.

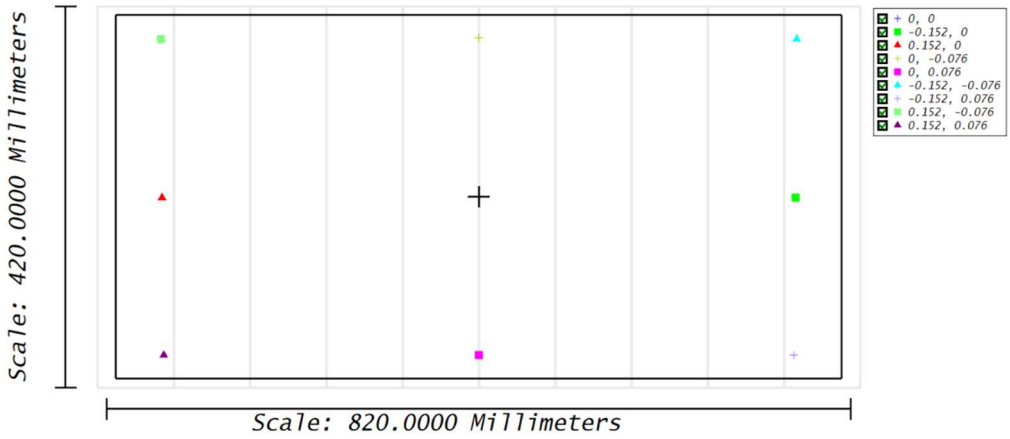

Fig. 18 Footprint diagram at image position for different field points

Fig. 19. represent footprint diagrams at multiple optical surfaces and for multiple field points, illustrating how the beam evolves as it propagates through the telescope.

(a) Primary mirror

The footprint clearly reproduces the segmented hexagonal geometry of the JWST primary mirror. The high and uniform ray coverage across the segments, together with a reported throughput of ~80%, indicates efficient pupil illumination with expected losses due to segmentation gaps and obscurations.

(b) Secondary mirror

The footprint is slightly shifted and clipped relative to the circular secondary aperture. The displacement of differently colored footprints reflects off-axis field points, while their containment within the mirror boundary confirms proper sizing and alignment of the secondary mirror without significant vignetting.

(c) Tertiary mirror

Here, footprints from different field points are spatially separated into distinct regions on the tertiary mirror (with rectangular aperture). This separation is characteristic of the JWST layout and demonstrates how field angles map to different zones of the tertiary, an important consideration for surface quality and stray-light control.

(d) Fine Steering Mirror (FSM)

The combined footprints from all field points remain well contained within the FSM aperture. This confirms that the FSM "sees" the full telescope pupil for all considered fields, validating its sizing and ensuring effective image stabilization and fine pointing control.

Overall, these footprint diagrams verify proper beam propagation, correct optical sizing, absence of field-dependent vignetting, and consistent pupil coverage throughout the JWST Optical Telescope Element, from the segmented primary mirror to the fine steering mirror.

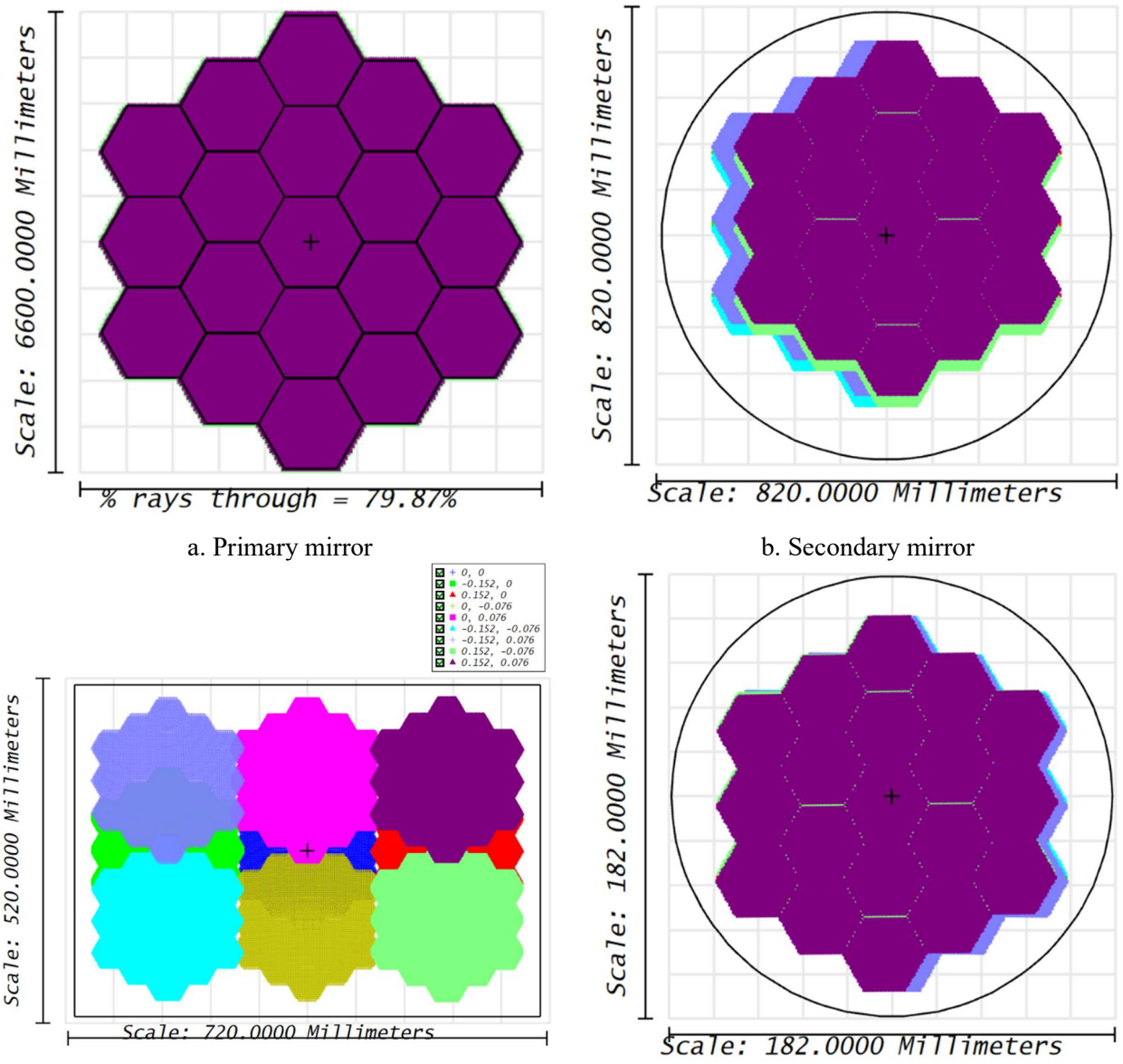

a. Primary mirror

b. Secondary mirror

c. Tertiary mirror

d. FSM position

Fig. 19. Footprint diagrams for different surface position on JWST for different field points

3.2 Analysis of spot diagrams

Spot diagrams are graphical representations of where rays from a point source intersect the image plane (or an intermediate surface) after propagating through an optical system. They show the distribution and shape of ray intersections for different field points and wavelengths. In optical analysis, spot diagrams are used to evaluate image quality, identify residual aberrations, and assess alignment and focus. By comparing the spot size and symmetry to the Airy disk or detector pixel size, they indicate whether the system operates in a diffraction-limited regime. Spot diagrams are therefore a fundamental tool for verifying optical performance, tolerances, and wavefront control in precision systems such as the James Webb Space Telescope.

The figure 20 presents spot diagrams for the James Webb Space Telescope (JWST) evaluated at the IMAGE surface for a set of nine rectangular field points distributed symmetrically across the field of view. Each sub-panel corresponds to a specific field angle, indicated above the plot (e.g., on-axis, ±0.152° in X, ±0.076° in Y, and their combinations). The black circle in each diagram represents the Airy disk, with an Airy radius of approximately 24.4 μm, providing a diffraction-limited reference. The colored ray clusters show the geometric

image of each field point relative to the chief ray. Across all field positions, the spots remain well contained within the Airy disk, indicating diffraction-limited performance over the evaluated field. The on-axis field exhibits the smallest and most symmetric spot, while off-axis fields show slightly increased spot size and mild asymmetry, consistent with residual off-axis aberrations. The reported RMS spot radii range from approximately 4.1 μm to 16.3 μm, and the geometric radii increase toward the edge of the field, reflecting the expected field-dependent behavior. Overall, spot diagrams demonstrate that JWST maintains excellent image quality and effective wavefront control across its field of view at the image plane location.

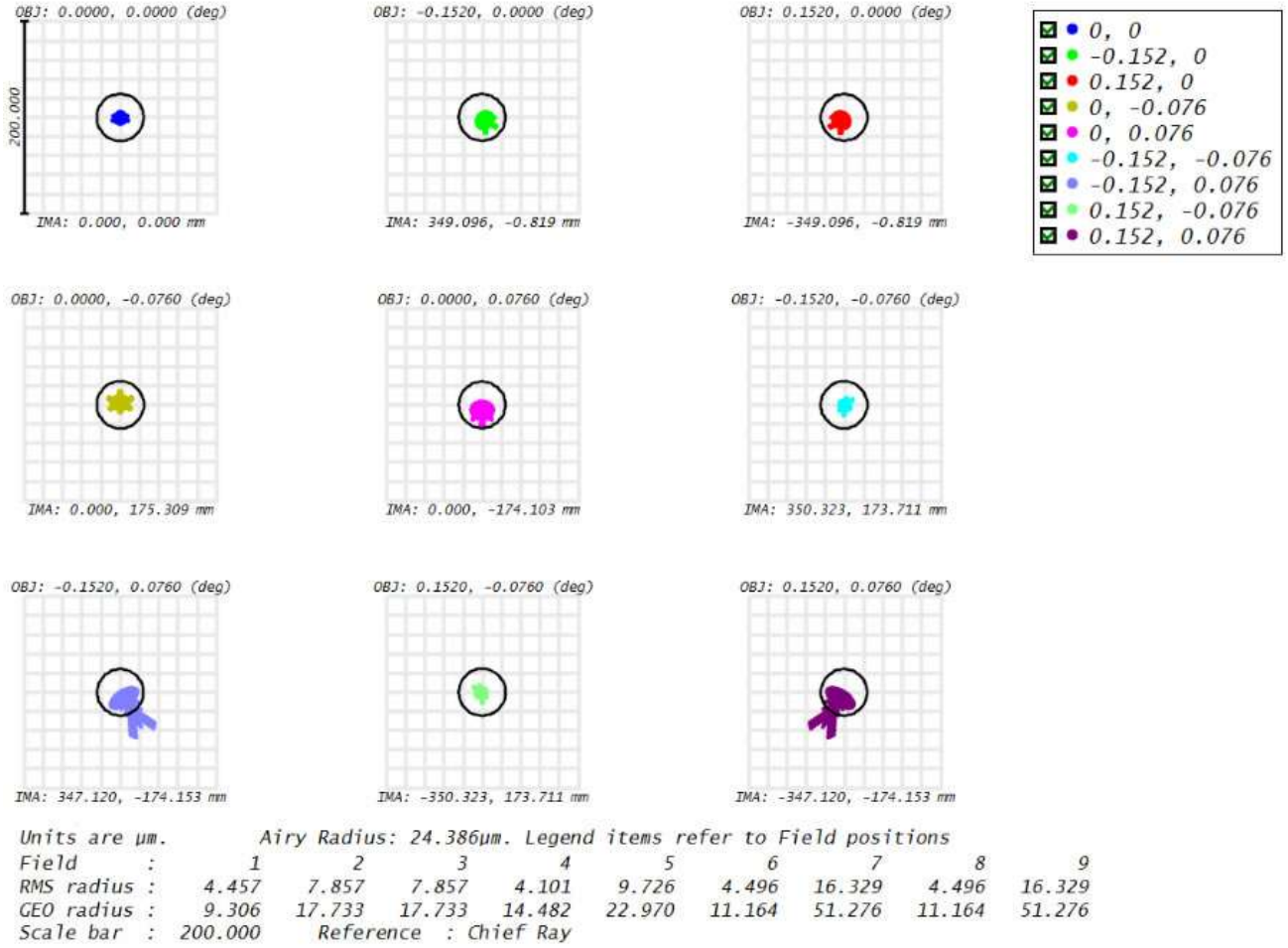

Fig. 20 Spot diagrams for the image plane position on JWST OTE for different fields

3.3 Analysis of wavefront error (WFE)

The wavefront function describes the deviation of an actual optical wavefront from an ideal reference wavefront (usually a perfect sphere or plane) as light propagates through an optical system. It represents the optical path difference (OPD) across the exit pupil and is commonly expressed in units of wavelength. Spatial variations in the wavefront function directly determine how phase errors are distributed over the pupil and how they affect image formation.

The Wavefront Error (WFE) is a quantitative measure derived from the wavefront function and characterizes the overall optical quality of the system. It is typically reported as root-mean-square (RMS) WFE, which provides a statistically robust metric of the accumulated phase errors across the pupil. Low RMS WFE indicates that the wavefront closely matches the ideal shape, resulting in high image sharpness and contrast, while higher WFE leads to blurred images, reduced Strehl ratio, and degraded modulation transfer function (MTF).

In diffraction-limited optical systems, such as the James Webb Space Telescope, strict WFE requirements are imposed to ensure near-ideal performance. A commonly used criterion is the Maréchal condition, which states that an optical system is diffraction-limited when the RMS WFE is smaller than approximately $\lambda/14$. Maintaining low WFE is therefore essential for achieving high Strehl ratios, stable point spread functions, and reliable scientific measurements. For JWST, active wavefront sensing and control are used to continuously monitor and correct WFE, ensuring optimal performance across the operational wavelength range.

The figure 21 shows the wavefront function of the JWST optical system evaluated at the image plane for the on-axis field at a wavelength of 1.0 μm. The color map represents the optical path difference across the exit pupil in units of waves, mapped onto the segmented hexagonal pupil geometry of the primary mirror. The wavefront exhibits a smooth, radially symmetric structure, with minimal discontinuities between individual mirror segments, indicating good segment phasing and alignment. The peak-to-valley (P–V) wavefront error is approximately 0.102 waves, while the RMS wavefront error is 0.0249 waves, corresponding to about λ/40 at 1 μm. This level of RMS WFE comfortably satisfies the diffraction-limited criterion and implies a high Strehl ratio. Overall, wavefront function confirms that the JWST optical telescope element achieves excellent optical quality at the image plane, consistent with the mission's stringent wavefront error requirements and its ability to deliver near-diffraction-limited performance across its operational wavelength range.

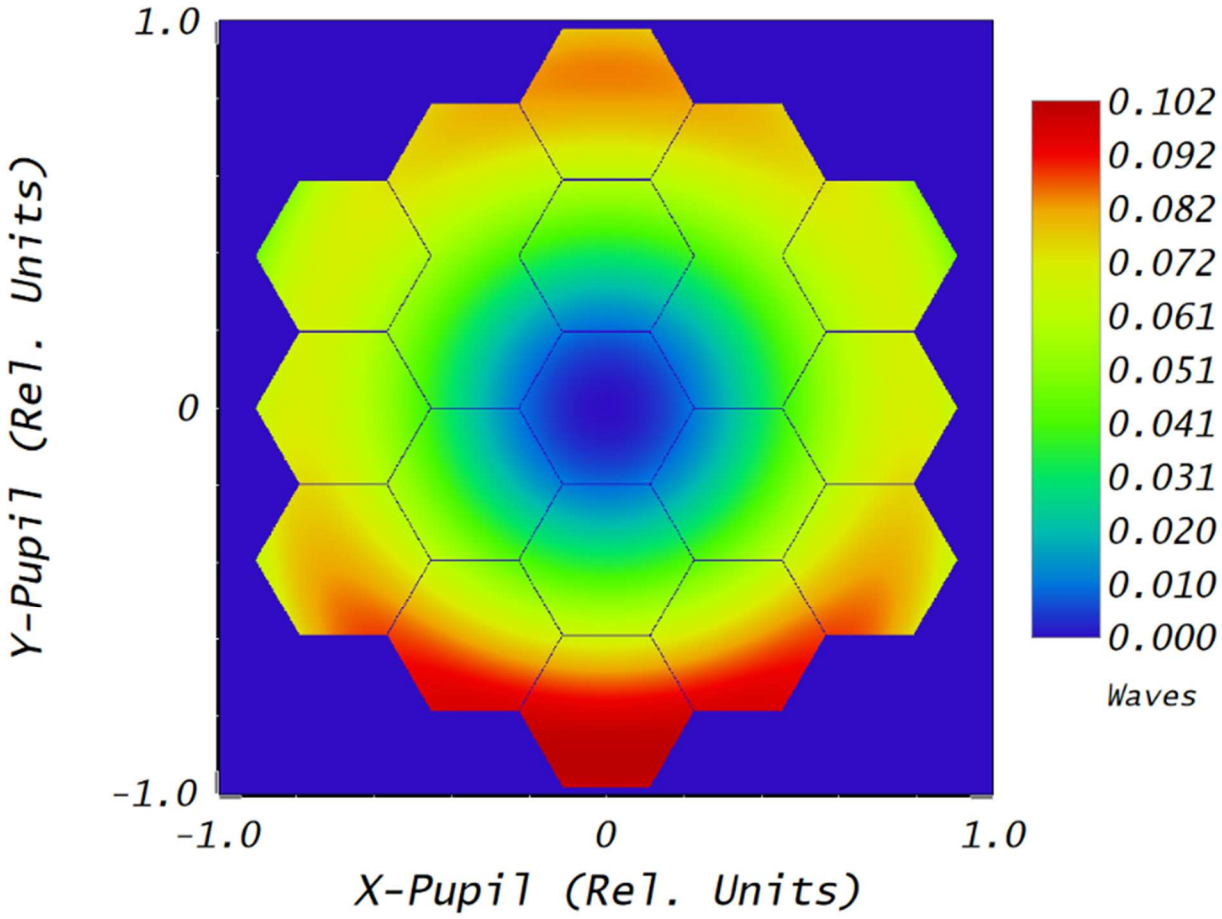

Fig. 21 Wavefront function of the JWST optical system evaluated at the IMAGE surface for an off-axis field angle of 0.125° and a wavelength of 0.74 μm.

3.4 Analysis of point spread function (PSF) and Strehl ratio

The point spread function (PSF) describes how an optical system images an ideal point source, such as a distant star. Instead of being focused into a perfect point, light is distributed over a finite area due to diffraction, optical aberrations, and pupil geometry. The PSF therefore represents the fundamental response of the optical system and fully characterizes its image-forming performance. In optical analysis and telescope design, the PSF is used to quantify image quality, resolution, and contrast. Its shape and intensity distribution reveal the effects of diffraction, central obscuration, segmented pupils, and residual wavefront errors. Key performance metrics such as Strehl ratio, encircled energy, modulation transfer function (MTF), and resolving power are all derived directly from the PSF.

For systems like the James Webb Space Telescope, the PSF is especially important because it reflects the combined effects of segmented primary mirrors, wavefront sensing and control, and alignment accuracy. Accurate PSF modeling and measurement are essential for verifying diffraction-limited performance, predicting scientific image quality, and supporting post-processing techniques such as deconvolution in astronomical observations.

The figure 22 shows the logarithmic FFT point spread function (PSF) of the JWST optical system evaluated at the image plane, for an on-axis field (0°, 0°) and a wavelength of 1 μm. The bright central peak represents the diffraction-limited core of the PSF, where most of the optical energy is concentrated. Its high intensity and symmetry indicate good optical alignment and effective wavefront control. Surrounding the core, a complex pattern of diffraction rings and spikes is visible. These structures arise from the segmented hexagonal primary mirror, the central obscuration, and the support geometry, all of which imprint characteristic interference features into the PSF. The cross-like and hexagonally modulated diffraction features reflect the JWST pupil geometry, including segment edges and gaps, while the use of a logarithmic intensity scale reveals low-level sidelobes spanning several orders of magnitude below the peak intensity. This confirms that, although faint diffraction artifacts are present, the majority of the energy remains tightly confined near the optical axis. Overall, the PSF demonstrates that JWST achieves near-ideal diffraction-limited performance at 1 μm, with a well-defined central core and predictable diffraction structure consistent with its segmented aperture design.

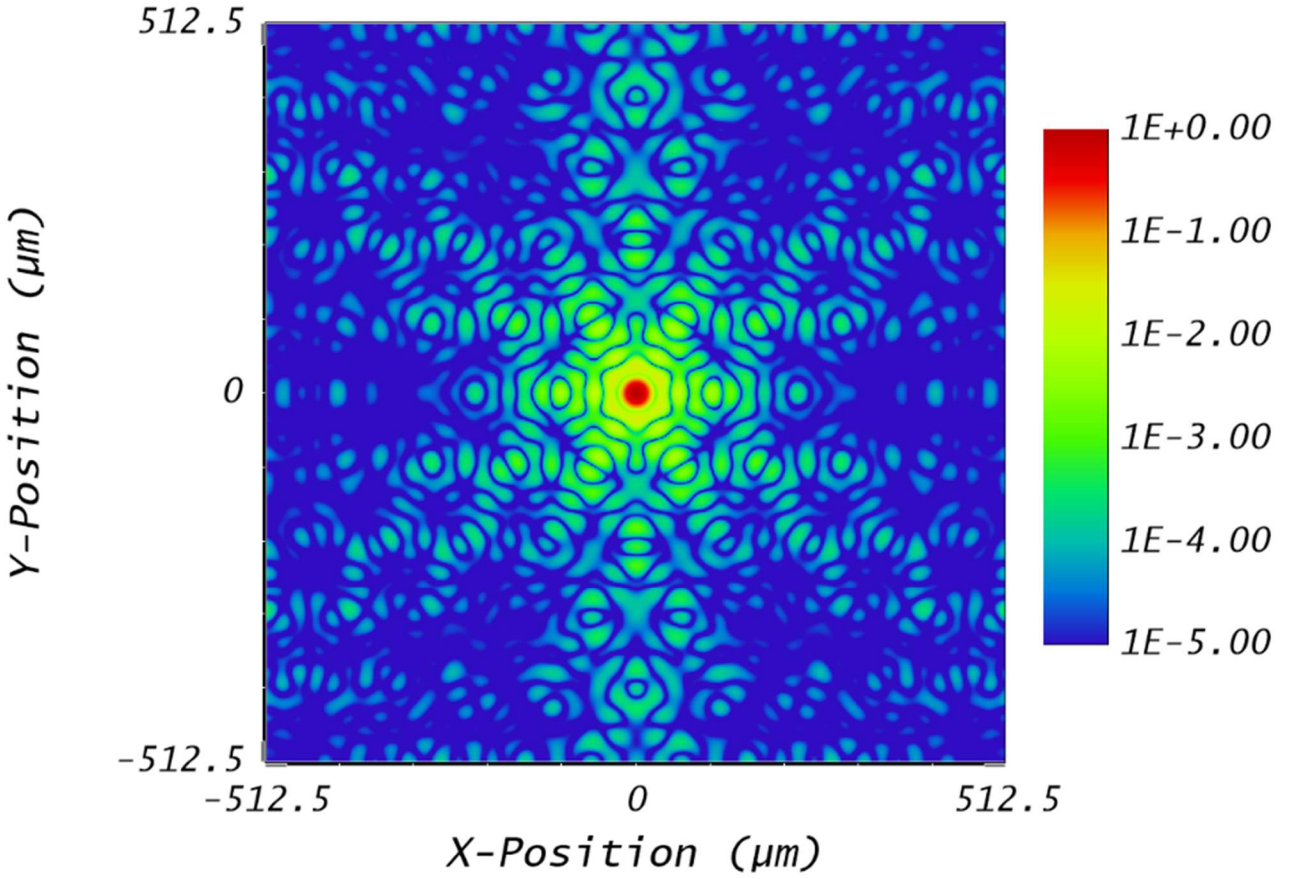

Fig. 22 Logarithmic FFT point spread function (PSF) of the JWST optical system, evaluated at image surface, for a wavelength of 1 μm and on axis field (0°,0°)

To determine Strehl ratio, Huygens point spread function (PSF) was used. Generally, the Huygens PSF is computed by directly propagating the optical field from the pupil to the image plane, fully preserving phase information and diffraction effects, which makes it highly accurate for evaluating image quality and Strehl ratio. In contrast, the FFT PSF (i.e. earlier diagram, Fig. 22) is obtained by Fourier transforming the pupil function on a sampled grid, offering much faster computation but with accuracy limited by sampling, window size, and numerical approximations. Consequently, the Huygens PSF is preferred for final performance verification, while the FFT PSF is mainly used for rapid analysis and qualitative assessment.

The figure 23 presents the polychromatic Huygens point spread function (PSF) of the JWST optical system evaluated at the image surface for a wavelength of 1 μm, shown for two different field positions. The upper plot corresponds to the on-axis field, where the PSF exhibits a sharp, narrow central peak with high symmetry. Strehl ratio here is 0.976. The high peak intensity and compact core indicate excellent optical alignment and minimal wavefront error, consistent with diffraction-limited performance. Energy is strongly concentrated in the central lobe, with only weak surrounding diffraction rings. The lower plot shows the PSF for on off-axis field point (see Fig. 16). Strehl ratio here is 0.874. While the central peak remains well defined, it is slightly reduced in

height and accompanied by more pronounced asymmetric diffraction features. This behavior reflects the influence of off-axis aberrations, field curvature, and pupil geometry effects. Nevertheless, the PSF remains compact, demonstrating that image quality degradation across the field is well controlled. Overall, the comparison confirms that JWST maintains high Strehl ratio and near diffraction-limited performance both on-axis and off-axis, with only moderate and predictable changes in the PSF shape toward the field edges.

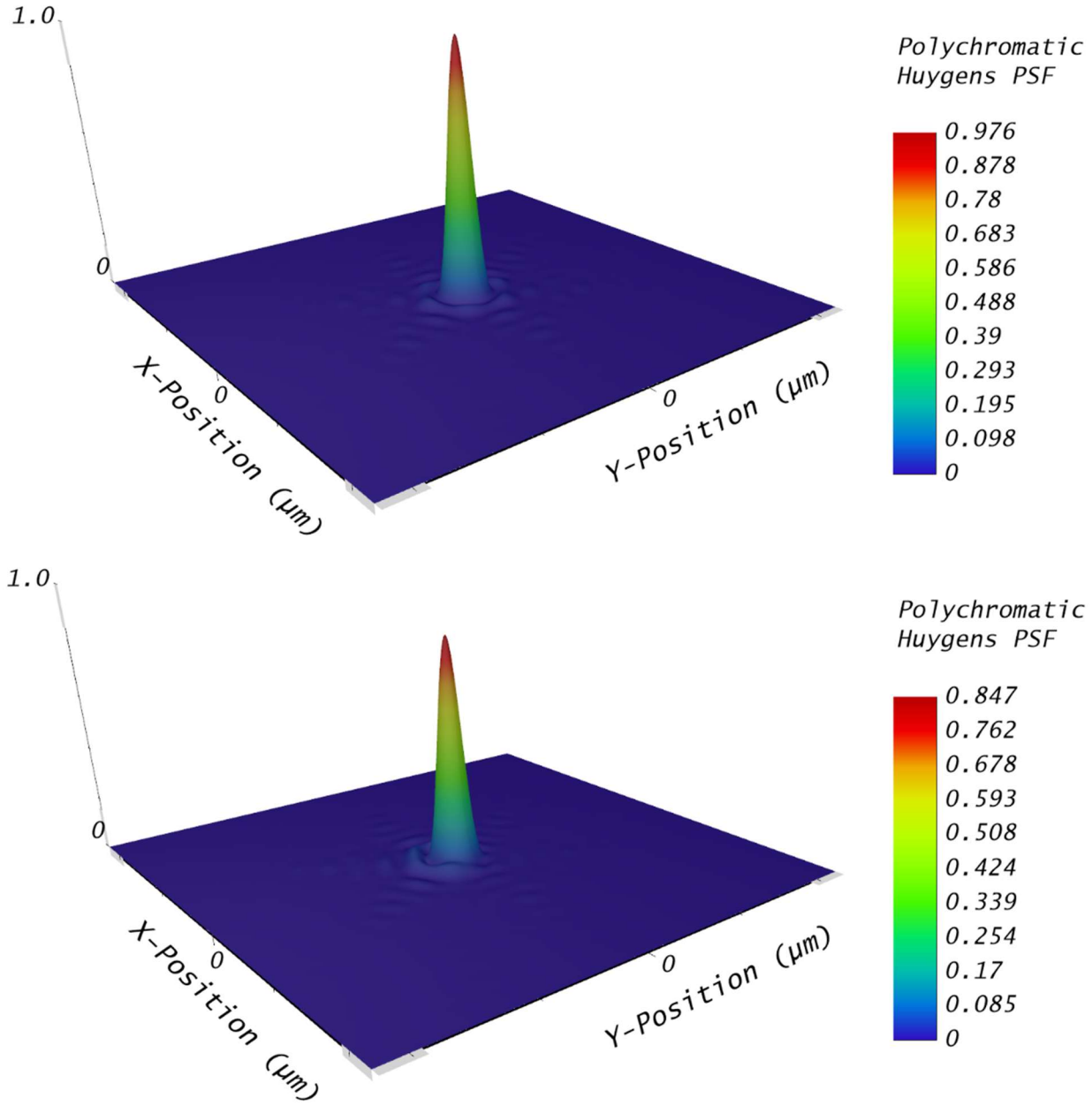

Fig. 23 Polychromatic Huygens point spread function (PSF) of the JWST optical system evaluated at a image surface for wavelength of 1 µm and two different fields - on axis (upper image) and off-axis (lower image)

3.5 Analysis of encircled energy (EE)

Encircled Energy (EE) is a quantitative measure of how optical energy from a point source is distributed in the image plane. It represents the fraction of the total point spread function (PSF) energy contained within a circular aperture of a given radius, centered on the image centroid.

Mathematically, EE is obtained by integrating the PSF intensity from the center outward and normalizing it to the total energy. The result is typically presented as an EE curve, showing the percentage of energy enclosed as a function of radius.

Encircled Energy is widely used to evaluate image sharpness, optical alignment, and system performance, especially in space telescopes such as JWST. It provides a direct metric for determining how much light is

concentrated within a detector pixel or within a specified radius (e.g., the Airy disk), and is therefore essential for verifying diffraction-limited performance and meeting scientific imaging requirements.

Encircled Energy for JWST, presented in Fig. 24, is calculated based on the diffraction PSF rather than purely geometric ray tracing. It uses either the FFT PSF or Huygens PSF to determine the true intensity distribution in the image plane, including the effects of wave interference and wavefront error. Computationally, first the complex pupil function is calculated, which includes both amplitude and phase (wavefront error). Then a Fourier transform (FFT method) or a direct Huygens integration is performed to obtain the PSF intensity distribution at the image plane. The Encircled Energy is then determined by integrating the PSF intensity within a circular radius centered on the image centroid. This approach accounts for diffraction effects, central obstruction, segmentation, and wavefront aberrations, making it the correct method for evaluating diffraction-limited systems such as JWST.

Figure 24 shows the polychromatic FFT diffraction encircled energy for the JWST optical system at the image plane, evaluated for multiple field points across the field of view (see Fig. 16). Curves represent the fraction of total energy enclosed as a function of radius from the image centroid, with the diffraction limit included for comparison. The results indicate that JWST concentrates energy very efficiently: 78.9% of the total energy is enclosed within Airy disk radius (recall that Airy disk radius is 24.4 μm for JWST) for all evaluated field points. Encircled energy is 80% at radial distance of 34 μm, around 40 μm the encircled energy reaches roughly 85% and it gradually approaches 100% beyond ~150-200 μm. The close agreement between the field-dependent curves and the diffraction-limit curve shows that the system remains near diffraction-limited across the full field, with only minor field-dependent degradation. Overall, the graph confirms excellent image quality and uniform performance over the field of view, consistent with JWST's diffraction-limited design requirements.

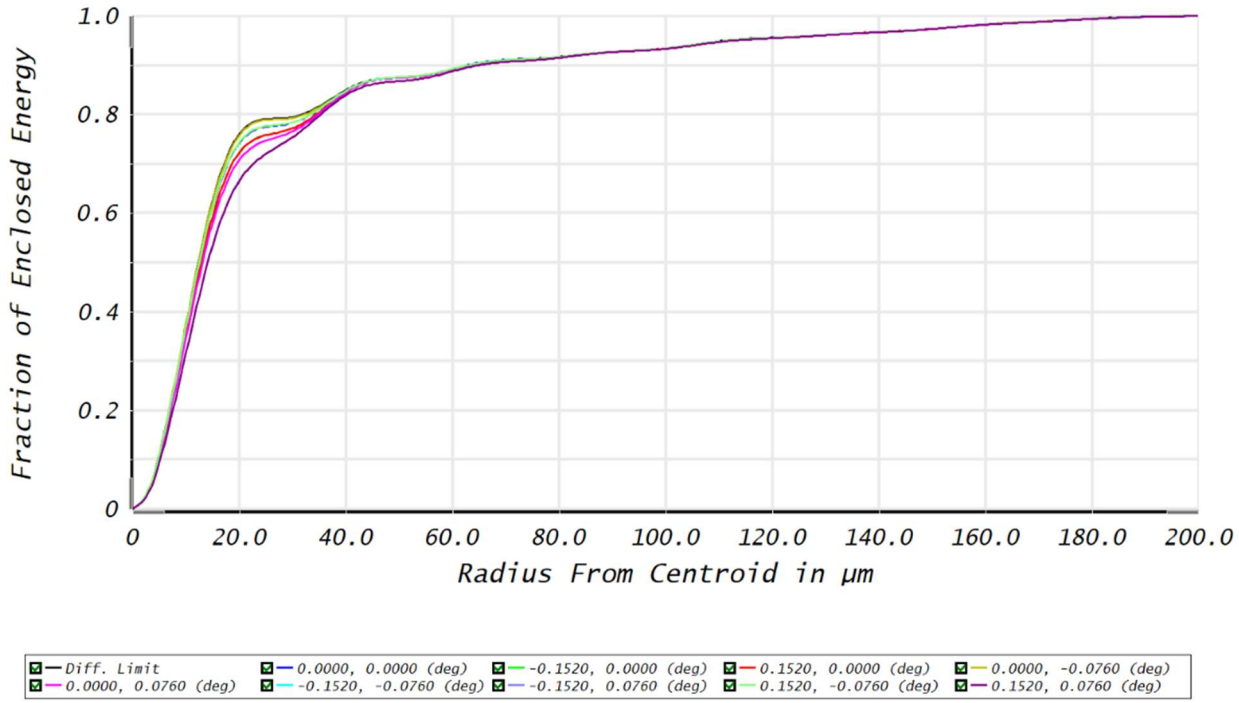

Fig. 24 Polychromatic FFT diffraction encircled energy (EE) for the JWST optical system at the image plane, evaluated for multiple field points across the field of view

3.6 Analysis of modulation transfer function (MTF)

The Modulation Transfer Function (MTF) is a fundamental metric used to quantify the imaging performance of an optical system. It describes how effectively the system transfers contrast from the object to the image as a function of spatial frequency. In practical terms, MTF indicates how well fine details of different sizes are preserved after passing through the optical system.

Mathematically, the MTF is the magnitude of the Optical Transfer Function (OTF), which is the Fourier transform of the Point Spread Function (PSF). While the PSF describes how a single point source is imaged, the MTF characterizes the system's response to sinusoidal patterns of varying spatial frequencies (measured in cycles per millimeter or cycles per degree).

An ideal diffraction-limited system exhibits an MTF curve that decreases smoothly from unity at zero spatial frequency (perfect contrast for large features) to zero at the cutoff frequency, which defines the system's resolution limit. Any deviation from the diffraction limit - due to aberrations, misalignment, or surface errors - reduces the MTF, particularly at mid- and high-spatial frequencies.

For systems such as the James Webb Space Telescope (JWST), the MTF is a critical indicator of diffraction-limited performance. A close agreement between the actual MTF and the diffraction-limited curve confirms high optical quality, effective wavefront control, and the ability to resolve fine structures with high contrast.

The figure 25 shows the polychromatic Modulation Transfer Function (MTF) of the JWST optical system for multiple field points and for both tangential and sagittal directions. The vertical axis represents the modulus of the Optical Transfer Function (OTF), while the horizontal axis shows spatial frequency in cycles per millimeter. At zero spatial frequency, the MTF starts at 1.0, indicating perfect contrast transfer for large-scale image features. As spatial frequency increases, the MTF gradually decreases, reflecting the reduced ability of the system to reproduce fine details. The curves approach zero near the cutoff frequency (around 50 cycles/mm), which defines the resolution limit of the system. The solid and dashed curves correspond to tangential and sagittal components at different off-axis field positions (e.g., 0°, ±0.152°, ±0.076°). The close grouping of these curves indicates very small variation across the field, demonstrating good field uniformity and minimal astigmatism. Furthermore, the actual system curves closely follow the diffraction-limited curves, confirming that JWST operates near the diffraction limit over the evaluated field points. Overall, the graph shows that JWST maintains high contrast transfer across a wide range of spatial frequencies, with only minor degradation off-axis, consistent with excellent optical alignment and effective wavefront control.

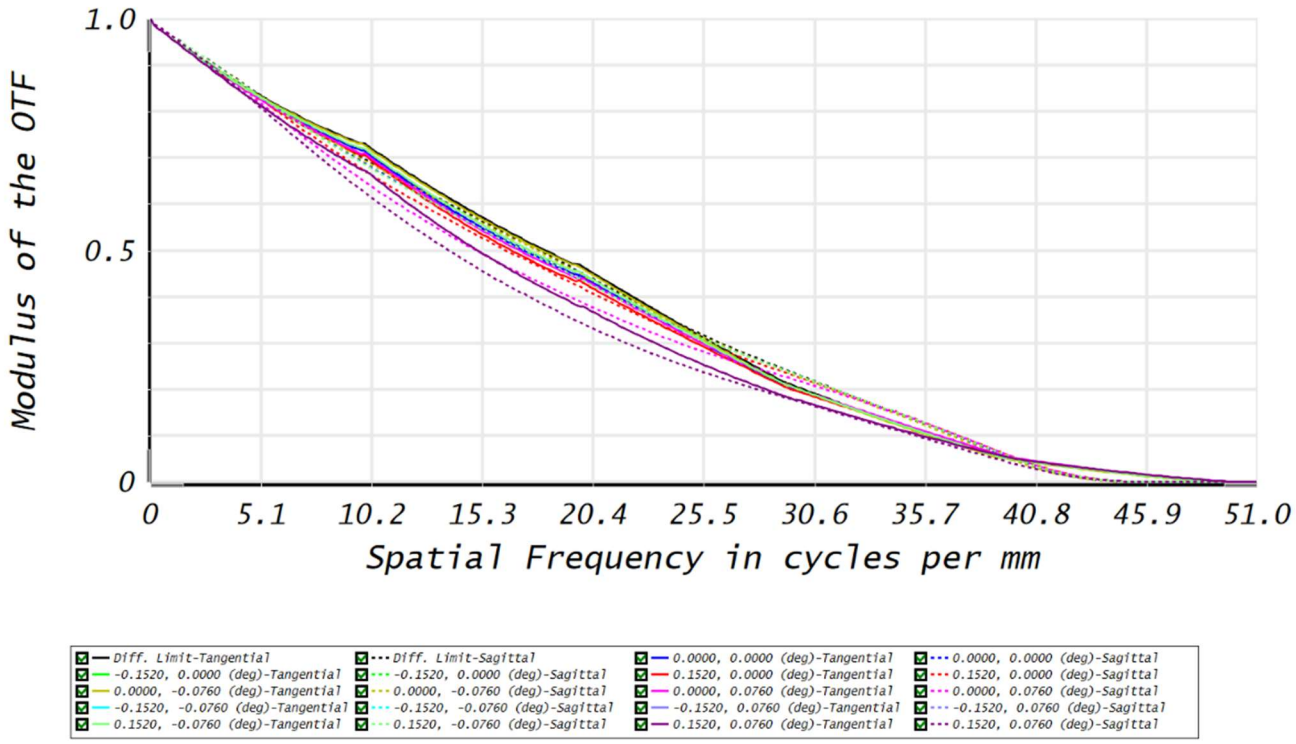

Fig. 25 The polychromatic modulation transfer function (MTF) of the JWST optical system for multiple field points and for both tangential and sagittal directions

3.7 Segment misalignment analysis

To determine the optical performance parameters of the James Webb Space Telescope (JWST) under realistic on-orbit conditions, a segmented mirror modeling approach was employed in this paper. In this method, each primary mirror segment is modeled individually using a User-Defined Aperture (UDA) file, enabling precise representation of the segmented pupil geometry.After defining the nominal optical configuration, controlled perturbations can be introduced to simulate realistic in-space misalignments. These perturbations include rigid-body motions such as piston (axial displacement), tip, and tilt of individual mirror segments. By applying these degrees of freedom independently to each segment, one can replicate wavefront errors arising from thermal distortions, deployment tolerances, or long-term structural drift in the space environment. This approach enables

systematic evaluation of resulting optical performance metrics, including wavefront error, point spread function degradation, encircled energy variation, and modulation transfer function changes. Consequently, the model provides a realistic framework for assessing alignment sensitivity, segment phasing tolerances, and overall system robustness of the JWST under operational conditions.

As a first step, in the Non-Sequential Component Editor (Fig. 26), the JWST primary mirror was modeled as an array of hexagonal reflective segments (hex1 - hex19). Each segment was implemented as a Standard Surface with a MIRROR property and a User-Defined Aperture (UDA) to impose the hexagonal pupil geometry, while sharing the same primary-mirror base conic (radius and conic constant). A sufficiently large maximum aperture (3500 mm) was used to avoid numerical clipping of the UDA-defined segment boundaries

	Object Type	Comment	Ref Object	Inside Of	X Position	Y Position	Z Position	Tilt About X	Tilt About Y	Tilt About Z	Material	Radius	Conic	Maximum Aper	Minimum Aper
1	Standard Surface	hex1	0	0	0.000	0.000	600.000	0.000	0.000	0.000	MIRROR	-1.588E+04	-0.997	3500.000	0.000
2	Standard Surface	hex2	0	0	0.000	0.000	600.000	0.000	0.000	0.000	MIRROR	-1.588E+04	-0.997	3500.000	0.000
3	Standard Surface	hex3	0	0	0.000	0.000	600.000	0.000	0.000	0.000	MIRROR	-1.588E+04	-0.997	3500.000	0.000
4	Standard Surface	hex4	0	0	0.000	0.000	600.000	0.000	0.000	0.000	MIRROR	-1.588E+04	-0.997	3500.000	0.000
5	Standard Surface	hex5	0	0	0.000	0.000	600.000	0.000	0.000	0.000	MIRROR	-1.588E+04	-0.997	3500.000	0.000
6	Standard Surface	hex6	0	0	0.000	0.000	600.000	0.000	0.000	0.000	MIRROR	-1.588E+04	-0.997	3500.000	0.000
7	Standard Surface	hex7	0	0	0.000	0.000	600.000	0.000	0.000	0.000	MIRROR	-1.588E+04	-0.997	3500.000	0.000
8	Standard Surface	hex8	0	0	0.000	0.000	600.000	0.000	0.000	0.000	MIRROR	-1.588E+04	-0.997	3500.000	0.000
9	Standard Surface	hex9	0	0	0.000	0.000	600.000	0.000	0.000	0.000	MIRROR	-1.588E+04	-0.997	3500.000	0.000
10	Standard Surface	hex10	0	0	0.000	0.000	600.000	0.000	0.000	0.000	MIRROR	-1.588E+04	-0.997	3500.000	0.000
11	Standard Surface	hex11	0	0	0.000	0.000	600.000	0.000	0.000	0.000	MIRROR	-1.588E+04	-0.997	3500.000	0.000
12	Standard Surface	hex12	0	0	0.000	0.000	600.000	0.000	0.000	0.000	MIRROR	-1.588E+04	-0.997	3500.000	0.000
13	Standard Surface	hex13	0	0	0.000	0.000	600.000	0.000	0.000	0.000	MIRROR	-1.588E+04	-0.997	3500.000	0.000
14	Standard Surface	hex14	0	0	0.000	0.000	600.000	0.000	0.000	0.000	MIRROR	-1.588E+04	-0.997	3500.000	0.000
15	Standard Surface	hex15	0	0	0.000	0.000	600.000	0.000	0.000	0.000	MIRROR	-1.588E+04	-0.997	3500.000	0.000
16	Standard Surface	hex16	0	0	0.000	0.000	600.000	0.000	0.000	0.000	MIRROR	-1.588E+04	-0.997	3500.000	0.000
17	Standard Surface	hex17	0	0	0.000	0.000	600.000	0.000	0.000	0.000	MIRROR	-1.588E+04	-0.997	3500.000	0.000
18	Standard Surface	hex18	0	0	0.000	0.000	600.000	0.000	0.000	0.000	MIRROR	-1.588E+04	-0.997	3500.000	0.000
19	Standard Surface	hex19	0	0	0.000	0.000	600.000	0.000	0.000	0.000	MIRROR	-1.588E+04	-0.997	3500.000	0.000

Fig. 26 Non-sequential modeling of the JWST primary mirror as an array of hexagonal reflective segments using User-Defined Apertures (UDA) with a common primary conic surface (default X,Y,Z position and tilts)

The figure 27 shows the wavefront error (WFE) map of the JWST pupil for the case where a segment misalignment has been intentionally introduced. Specifically, a +0.5 μm piston (axial displacement in the Z-direction) was applied to mirror segment 2, while a -0.5 μm piston was applied to mirror segment 5.

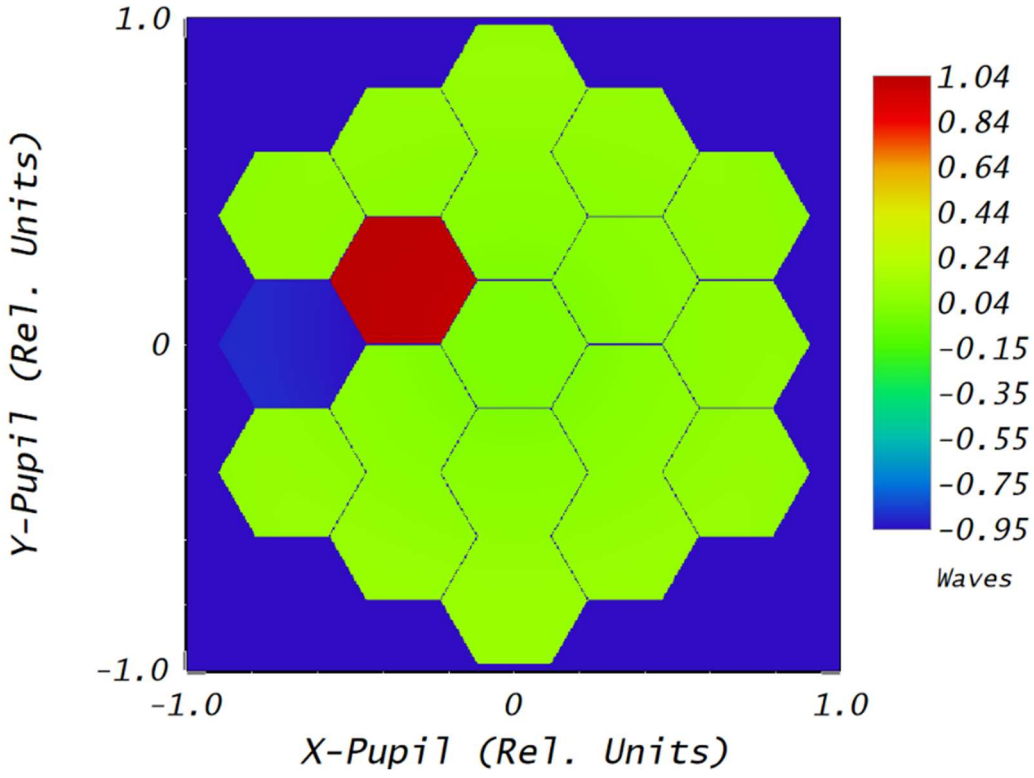

Fig. 27 The wavefront error (WFE) map of the JWST pupil for the case where a segment misalignment has been intentionally introduced (+0.5 μm piston (axial displacement in the Z-direction) was applied to mirror segment 2, while a -0.5 μm piston was applied to mirror segment 5).

The piston error, shown in Fig. 27, manifests as distinct phase discontinuities between the affected segments and the rest of the primary mirror. In the wavefront map, the segment 2 with positive piston appears in red (positive wavefront shift), while the segment 5 with negative piston appears in blue (negative wavefront shift), clearly indicating a relative optical path difference between them. The remaining segments are approximately uniform (green), showing that they remain properly phased. The piston term is dominant, while the residual coma aberration, although still present, is no longer visibly discernible in the diagram due to the overwhelming influence of the piston error. Spot diagrams are here almost unchanged (piston errors do not affect significantly ray trajectory). Quantitatively, the reported peak-to-valley (P-V) value of 1.9947 waves and RMS wavefront error of 0.3150 waves indicate degradation of optical performance. An RMS error of ~0.315 waves is far above the diffraction-limited criterion (typically ~0.07 waves RMS), meaning that the introduced ±0.5 μm piston misalignment significantly disrupts coherent interference across the segmented aperture. Such phase steps would strongly degrade the PSF, reduce Strehl ratio, and produce pronounced image artifacts, demonstrating the critical importance of precise segment phasing in JWST's segmented primary mirror system.

The next analysis examined the influence of segment tilt. Figure 28 presents screenshot of Non-Sequential Component Editor (NSCE) that can used to model the JWST segmented primary mirror.

	Object Type	Comment	Ref Object	Inside Of	X Position		Y Position	
1	Null Object	pivot hex 1	0	0	-2250.0000...		1299.038000	
2	Standard Surface	hex 1	1	0	2250.000000	P	-1299.0380...	P
3	Null Object	pivot hex 2	0	0	-2250.0000...		0.000000	
4	Standard Surface	hex 2	3	0	2250.000000	P	0.000000	P
5	Null Object	pivot hex 3	0	0	-2250.0000...		-1299.0380...	
6	Standard Surface	hex 3	5	0	2250.000000	P	1299.038000	P
7	Null Object	pivot hex 4	0	0	-1125.0000...		1948.557000	
8	Standard Surface	hex 4	7	0	1125.000000	P	-1948.5570...	P
9	Null Object	pivot hex 5	0	0	-1125.0000...		649.519000	
10	Standard Surface	hex 5	9	0	1125.000000	P	-649.519000	P
11	Null Object	pivot hex 6	0	0	-1125.0000...		-649.519000	
12	Standard Surface	hex 6	11	0	1125.000000	P	649.519000	P
13	Null Object	pivot hex 7	0	0	-1125.0000...		-1948.5570...	
14	Standard Surface	hex 7	13	0	1125.000000	P	1948.557000	P
15	Null Object	pivot hex 8	0	0	0.000000		2598.076000	
16	Standard Surface	hex 8	15	0	0.000000	P	-2598.0760...	P
17	Null Object	pivot hex 9	0	0	0.000000		1299.038000	
18	Standard Surface	hex 9	17	0	0.000000	P	-1299.0380...	P
19	Null Object	pivot hex 10	0	0	0.000000		0.000000	
20	Standard Surface	hex 10	19	0	0.000000	P	0.000000	P
21	Null Object	pivot hex 11	0	0	0.000000		-1299.0380...	
22	Standard Surface	hex 11	21	0	0.000000	P	1299.038000	P
23	Null Object	pivot hex 12	0	0	0.000000		-2598.0760...	
24	Standard Surface	hex 12	23	0	0.000000	P	2598.076000	P
25	Null Object	pivot hex 13	0	0	1125.000000		1948.557000	
26	Standard Surface	hex 13	25	0	-1125.0000...	P	-1948.5570...	P
27	Null Object	pivot hex 14	0	0	1125.000000		649.519000	
28	Standard Surface	hex 14	27	0	-1125.0000...	P	-649.519000	P
29	Null Object	pivot hex 15	0	0	1125.000000		-649.519000	
30	Standard Surface	hex 15	29	0	-1125.0000...	P	649.519000	P
31	Null Object	pivot hex 16	0	0	1125.000000		-1948.5570...	
32	Standard Surface	hex 16	31	0	-1125.0000...	P	1948.557000	P
33	Null Object	pivot hex 17	0	0	2250.000000		1299.038000	
34	Standard Surface	hex 17	33	0	-2250.0000...	P	-1299.0380...	P
35	Null Object	pivot hex 18	0	0	2250.000000		0.000000	
36	Standard Surface	hex 18	35	0	-2250.0000...	P	0.000000	P
37	Null Object	pivot hex 19	0	0	2250.000000		-1299.0380...	
38	Standard Surface	hex 19	37	0	-2250.0000...	P	1299.038000	P

Fig. 28 Non-Sequential Component Editor configuration for modeling JWST segmented primary mirror

In the Fig. 28, the mirror is represented as an array of 19 hexagonal segments, each implemented as a Standard Surface with mirror properties. For every segment ("hex 1" to "hex 19"), a corresponding Null Object ("pivot hex") is defined to serve as a local coordinate reference, enabling independent tilt adjustments. The X and Y Position columns specify the lateral placement of each segment, forming the characteristic hexagonal tiling pattern of the JWST primary mirror. Each mirror surface is referenced to its their pivot object, so any applied misalignment directly affects the associated segment.

The Fig. 29 shows the wavefront error (WFE) map of the JWST segmented primary mirror with mirror 8 tilted 0.0001° about Y axis, evaluated at the image plane for a wavelength of 1.0 μm and an on-axis field (0°, 0°). The map is displayed in normalized pupil coordinates (X-Pupil and Y-Pupil in relative units), revealing the hexagonal segmentation pattern of the 18 primary mirror segments. The dominant feature is a localized region of large positive wavefront error (red-yellow area) concentrated on the upper central segment. It indicates that this particular segment (mirror 8) was misaligned relative to others - due to segment tilt. The rest of the pupil shows similar wavefront error (blue region), showing that the misalignment is isolated to a single segment rather than a global aberration. Quantitatively, for this setup, the peak-to-valley (PV) wavefront error is 2.4688 waves and the RMS wavefront error is 0.2207 waves. An RMS error of this magnitude is well above the diffraction-limited criterion (typically ~λ/14 ≈ 0.07 waves RMS), meaning the system performance in this state would be significantly degraded. The localized wavefront discontinuity at the segment boundary would introduce strong phase errors, reducing Strehl ratio and image quality. This plot therefore illustrates the sensitivity of JWST optical performance to individual segment misalignment and shows the importance of precise segment phasing.

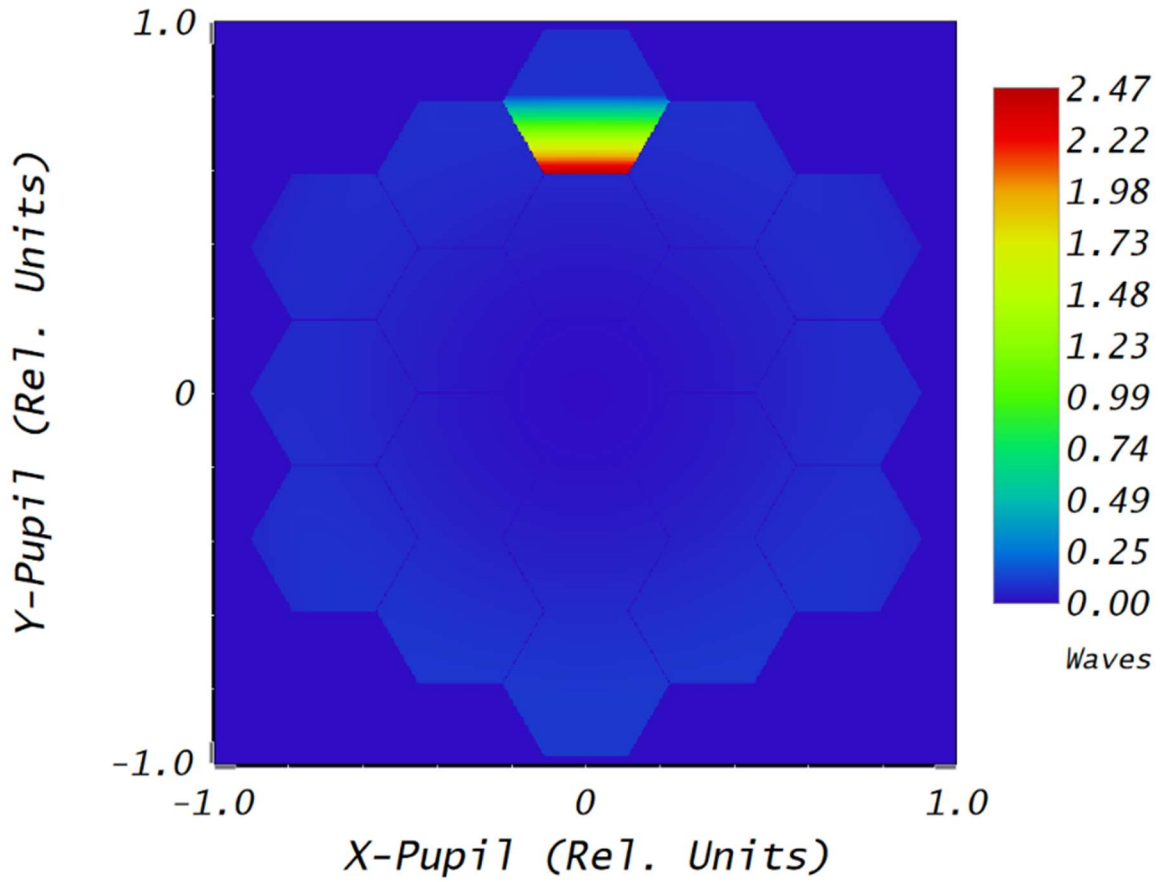

Fig. 29 The wavefront error (WFE) map of the JWST segmented primary mirror with mirror 8 tilted 0.0001° about Y axis, evaluated at the image plane for a wavelength of 1.0 μm and an on-axis field (0°, 0°)

The Fig. 30 shows spot diagrams for multiple field positions of the JWST optical system under the segment misalignment condition (mirror 8 was tilted 0.0001° about Y axis). The central circular outline represents the Airy disk, while the colored ray intersections show the actual geometric spot distribution. The coordinates below each subplot (IMA values) indicate the image height in millimeters for that field point. Rays from tilted segment (mirror 8) can be seen in lower part of diagrams, indicating separation from the rest of spots. It is important to note that spot diagrams alone are insufficient to evaluate segmented telescope phasing errors; wavefront and PSF analysis are required for a complete assessment of optical performance.

Fig. 30 Spot diagrams for multiple field positions of the JWST optical system under the segment misalignment condition (mirror 8 tilted 0.0001° about Y axis)

4. Conclusions

This study analyzed the optical performance of the James Webb Space Telescope using its published optical prescription and segmented mirror configuration. Geometric and diffraction-based analyses confirm that the nominal JWST optical system operates near the diffraction limit, achieving low RMS wavefront error, high Strehl ratio, efficient encircled energy concentration, and strong modulation transfer performance across the evaluated field. Footprint and spot diagram analyses verify correct beam propagation, absence of vignetting, and uniform image quality. Wavefront and PSF results demonstrate that the segmented primary mirror, when properly phased, behaves as a coherent monolithic aperture. Diffraction patterns clearly reflect the hexagonal segmentation geometry but remain well confined within the Airy disk envelope.

Segment misalignment simulations reveal the high sensitivity of system performance to piston and tilt errors. Even submicrometer-scale piston offsets or very small angular tilts introduce significant wavefront discontinuities, increasing RMS WFE well beyond diffraction-limited criteria and reducing image quality. These results quantitatively demonstrate the necessity of JWST's active wavefront sensing and control system. Overall, the analysis confirms that JWST's three-mirror anastigmat architecture, segmented beryllium primary mirror, and active alignment strategy successfully achieve the stringent optical requirements for diffraction-limited infrared astronomy. The presented modeling framework also provides a practical methodology for evaluating alignment sensitivity and performance margins in large segmented space telescopes.

Declaration of competing interest

The authors declare that they have no known financial or non-financial competing interests in any material discussed in this paper.

Funding information

No funding was received from any financial organization to conduct this research.

References

[1] P. Y. Bely *et al*., "Genesis of the James Webb Space Telescope architecture: The designers' story," *J. Astron. Telesc. Instrum. Syst.*, vol. 11, no. 3, pp. 030901-1–030901-30, Jul.–Sep. 2025, doi: https://doi.org/10.1117/1.JATIS.11.3.030901.

[2] L. D. Feinberg *et al*., "James Webb Space Telescope Optical Telescope Element mirror development history and results," in *Proc. SPIE Space Telescopes and Instrumentation 2012: Optical, Infrared, and Millimeter Wave*, vol. 8442, paper 84422B, 2012, doi: https://doi.org/10.1117/12.924271.

[3] M. Menzel *et al*., "The design, verification, and performance of the James Webb Space Telescope," *Publ. Astron. Soc. Pac.*, vol. 135, no. 1046, pp. 058002-1–058002-42, May 2023, doi: https://doi.org/10.1088/1538-3873/acbb9f.

[4] J. W. Contreras and P. A. Lightsey, "Optical design and analysis of the James Webb Space Telescope: Optical Telescope Element," in *Proc. SPIE Novel Optical Systems Design and Optimization VII*, vol. 5524, pp. 30–41, 2004, doi: https://doi.org/10.1117/12.559871.

[5] P. A. Lightsey *et al*., "James Webb Space Telescope: Large deployable cryogenic telescope in space," *Opt. Eng.*, vol. 51, no. 1, pp. 011003-1–011003-17, Jan. 2012, doi: https://doi.org/10.1117/1.OE.51.1.011003.

[6] M. W. McElwain *et al*., "The James Webb Space Telescope mission: Optical Telescope Element design, development, and performance," *Publ. Astron. Soc. Pac.*, vol. 135, no. 1046, pp. 058001-1–058001-42, May 2023, doi: https://doi.org/10.1088/1538-3873/acbb9f.

[7] Cloudy Nights Forum, "JWST in Zemax," Accessed: 2026. [Online]. Available: https://www.cloudynights.com/forums/topic/818241-jwst-in-zemax/

[8] P. A. Lightsey and Z. Wei, "James Webb Space Telescope stray light performance status update," in *Proc. SPIE Space Telescopes and Instrumentation 2012: Optical, Infrared, and Millimeter Wave*, vol. 8442, paper 84423B, 2012, doi: https://doi.org/10.1117/12.924852.

[9] S. O. Rohrbach *et al*., "Stray light modeling of the James Webb Space Telescope (JWST)," in *Proc. SPIE Space Telescopes and Instrumentation 2018: Optical, Infrared, and Millimeter Wave*, vol. 10698, paper 106981M, 2018, doi: https://doi.org/10.1117/12.2314061.

[10] D. S. Acton *et al*., "James Webb Space Telescope wavefront sensing and control algorithms," in *Proc. SPIE Optical, Infrared, and Millimeter Space Telescopes*, vol. 5487, pp. 887–896, 2004, doi: https://doi.org/10.1117/12.551846.

[11] H. P. Stahl, L. D. Feinberg, and S. C. Texter, "JWST primary mirror material selection," in *Proc. SPIE Optical, Infrared, and Millimeter Space Telescopes*, vol. 5487, pp. 818–824, 2004, doi: https://doi.org/10.1117/12.549582.

[12] P. A. Lightsey, A. A. Barto, and J. Contreras, "Optical performance for the James Webb Space Telescope," in *Proc. SPIE Optical, Infrared, and Millimeter Space Telescopes*, vol. 5487, pp. 825–832, 2004, doi: https://doi.org/10.1117/12.550091.

[13] M. D. Perrin *et al*., "James Webb Space Telescope Optical Simulation Testbed I: Overview and first results," in *Proc. SPIE Optical Engineering and Applications*, vol. 9143, paper 91430Z, 2014, doi: https://doi.org/10.1117/12.2056917.

[14] É. Choquet *et al*., "James Webb Space Telescope Optical Simulation Testbed II: Design of a three-lens anastigmat telescope simulator," in *Proc. SPIE Optical Engineering and Applications*, vol. 9143, paper 91430Z, 2014, doi: https://doi.org/10.1117/12.2056921.

[15] S. Egron *et al*., "James Webb Space Telescope Optical Simulation Testbed III: First experimental results with linear-control alignment," in *Proc. SPIE Space Telescopes and Instrumentation 2016*, vol. 9904, paper 99044A, 2016, doi: https://doi.org/10.1117/12.2233650.

[16] S. Egron *et al*., "James Webb Space Telescope Optical Simulation Testbed IV: Linear control alignment of the primary segmented mirror and the secondary mirror," in *Proc. SPIE Innovative Technologies and Concepts VIII*, vol. 10398, paper 1039811, 2017, doi: https://doi.org/10.1117/12.2272981.

[17] I. Laginja *et al*., "James Webb Space Telescope Optical Simulation Testbed V: Wide-field phase retrieval assessment," in *Proc. SPIE Space Telescopes and Instrumentation 2018*, vol. 10698, paper 106985U, 2018, doi: https://doi.org/10.1117/12.2313174.

[18] J. S. Knight *et al*., "Design of the master optical reference for the James Webb Space Telescope," in *Proc. SPIE Space Telescopes and Instrumentation 2014*, vol. 9143, paper 914306, 2014, doi: https://doi.org/10.1117/12.2057622.

[19] J. S. Knight *et al*., "Image quality verification analysis of the James Webb Space Telescope," in *Proc. SPIE Modeling, Systems Engineering, and Project Management for Astronomy IV*, vol. 7738, paper 77381Z, 2010, doi: https://doi.org/10.1117/12.858348.

[20] Space Telescope Science Institute, *James Webb Space Telescope Science Operations Concept Document (JWST-STScI-001157)*, Rev. A, Baltimore, MD, USA, 2011.

[21] Zemax LLC, "Designing of the James Webb Space Telescope," YouTube video. [Online]. Available: https://www.youtube.com/watch?v=OE3ZowuvAJY

[22] Zemax LLC, "JWST Part 2: Modeling the James Webb Telescope Segments in OpticStudio," YouTube video. [Online]. Available: https://www.youtube.com/watch?v=KNP2EEHM_8g